

Single-shot pressure-sensitive paint lifetime measurements on fast rotating blades using an optimized double-shutter technique

Armin Weiss¹  · Reinhard Geisler¹ · Till Schwermer¹ · Daisuke Yorita¹ · Ulrich Henne¹ · Christian Klein¹ · Markus Raffel¹

Received: 2 May 2017 / Revised: 12 July 2017 / Accepted: 14 July 2017 / Published online: 18 August 2017
© Springer-Verlag GmbH Germany 2017

Abstract A pressure-sensitive paint (PSP) system is presented to measure global surface pressures on fast rotating blades. It is dedicated to solve the problem of blurred image data employing the single-shot lifetime method. The efficient blur reduction capability of an optimized double-shutter imaging technique is demonstrated omitting error-prone post-processing or laborious de-rotation setups. The system is applied on Mach-scaled DSA-9A helicopter blades in climb at various collective pitch settings and blade tip Mach and chord Reynolds numbers ($M_{\text{tip}} = 0.29\text{--}0.57$; $Re_{\text{tip}} = 4.63\text{--}9.26 \times 10^5$). Temperature effects in the PSP are corrected by a theoretical approximation validated against measured temperatures using temperature-sensitive paint (TSP) on a separate blade. Ensemble-averaged PSP results are comparable to pressure-tap data on the same blade to within 250 Pa. Resulting pressure maps on the blade suction side reveal spatially high resolved flow features such as the leading edge suction peak, footprints of blade-tip vortices and evidence of laminar–turbulent boundary-layer (BL) transition. The findings are validated by a separately conducted BL transition measurement by means of TSP and numerical simulations using a 2D coupled Euler/boundary-layer code. Moreover, the principal ability of the single-shot technique to capture unsteady flow phenomena is stressed revealing three-dimensional pressure fluctuations at stall.

1 Introduction

Surface pressure measurements on rotating blades are vital to understand inherent flow phenomena (Gorton et al. 1995), for the characterization of aerodynamic loads and performance data (Lorber et al. 1989) and due to their inevitable use for the validation of computational fluid dynamics (CFD) codes used for prediction purposes (Hariharan et al. 2014). Benchmark experiments in rotorcraft research used for CFD validation either provide integral balance data only (Balch and Lombardi 1985) or employ wall tapings providing data at discrete point-wise locations (Lorber et al. 1989; Tung and Branum 1990). Pressure transducers installed in rotating blades introduce heavy centrifugal loads. The need to transfer data outside the rotating frame demands a costly telemetric solution. Due to limited space for installation, the spatial resolution is oftentimes quite scarce and characteristic flow features such as the suction peak or the footprints of the tip vortex can hardly be resolved, which complicates numerical validation (Yamauchi and Johnson 1995). Hence, pressure-sensitive paint (PSP) is a powerful technique as it non-intrusively provides global pressures on a coated model surface at high spatial resolution.

1.1 Pressure-sensitive paint principles

The PSP technique relies on photokinetic interactions between the airflow and a luminescent coating applied to the surface of interest. A detailed description and application examples of the technique are described by Bell et al. (2001) and Liu and Sullivan (2005). Being excited by light of a certain wavelength, the luminescent dye molecules emit light at a higher wavelength. This radiative process can be quenched by diffused oxygen depending on the local air pressure. For instance, higher local pressures reduce both

✉ Armin Weiss
armin.weiss@dlr.de
Reinhard Geisler
reinhard.geisler@dlr.de

¹ Institute of Aerodynamics and Flow Technology,
German Aerospace Center (DLR), Bunsenstr. 10,
37073 Göttingen, Germany

the amount of light emitted as well as the luminescent lifetime decay time. The emitted light does not only depend on pressure. In this regard, possible sources of uncertainty include spatially inhomogeneous excitation light and dye concentration as well as thermal quenching of luminescence and photo-degradation of the dye (Liu and Sullivan 2005). The luminescence is usually captured by a scientific grade camera using optical filters to separate the emitted signal from the excitation light. Using the “gated intensity ratio method” (Liu and Sullivan 2005) the lifetime is measured as a function of the ratio of two images I_{G1}/I_{G2} . They are subsequently recorded during the so-called “integration gates” $G1$ and $G2$. If both frames are acquired from a single excitation pulse, the method is referred to as the “single-shot lifetime technique” (Gregory et al. 2009; Juliano et al. 2011). With this approach any uncertainty originating from inhomogeneous or unstable pulsed excitation light is eliminated as the resulting pattern is the same in both images used for division. However, it is known that a residual spatial non-uniformity in the lifetime distribution persists even at uniform pressure (see Ruyten and Sellers 2006; Yorita et al. 2017). This in turn is accounted for by dividing the gated intensity ratio at any pressure p and temperature T (wind-on condition) by the ratio under known reference (ref) conditions, also referred to wind-off. The resulting ratio of ratios (RoR) can then be related to pressure, for instance by

$$\text{RoR} = \frac{\frac{I_{G1}}{I_{G2}}}{\frac{I_{G1}}{I_{G2}}_{\text{ref}}} = \frac{\frac{I_{G1}}{I_{G2}}_{\text{wind-on}}}{\frac{I_{G1}}{I_{G2}}_{\text{wind-off}}} = \sum_{i,k=0}^{m,n=2} a_{ik} \left(\frac{T}{T_{\text{ref}}} \right)^i \left(\frac{p}{p_{\text{ref}}} \right)^k, \quad (1)$$

where $a_{i,k}$ are calibration coefficients to be obtained.

1.2 PSP on rotating blades

A particular challenge related to PSP measurements on fast rotating blades is to capture sharp images at sufficient signal-to-noise ratio (SNR). A common approach is to accumulate up to several hundreds of phase-locked exposures on the image sensor using a pulsed excitation synched to the rotating blade. This phase-averaging technique has previously been applied to measure surface pressure on blades of a scale-model fan (Bencic 1997), a turbocharger compressor (Gregory 2004), a turbine rotor (Suryanarayanan et al. 2010) or on fast rotating propellers (Klein et al. 2013). The technique provides reproducible results if the position of the rotating blade in the image and the excitation pulses are perfectly stable. However, Wong et al. (2005, 2010) for instance reported significant smear in resultant images due to cycle-to-cycle lead-lag and flapping motion when testing helicopter rotor blades being susceptible to aero-elastic effects. Moreover, if pressure fluctuations are of interest the

phase-averaging accumulation technique is inherently limited to capture transient phenomena occurring in phase with the rotating frequency.

These limitations are overcome by using the single-shot lifetime technique as employed by Juliano et al. (2011), where both gated intensities are acquired from a single excitation pulse. To get sufficient signal a high energy light source such as a laser is required for paint excitation. Due to its self-referencing character, the single-shot lifetime technique is insensitive to errors originating from model movement within inhomogeneous illumination as laser speckles, for instance. Disotell et al. (2014) applied the method for unsteady PSP measurements on a small-scale fully articulated helicopter blade in forward flight. They employed a fast-responding PSP and took advantage of the single-shot technique to resolve unsteady pressure footprints of flow structures on the blade. The technique has recently matured to be used on the entire upper surface of large-scale helicopter blades (with ~ 1.7 m blade radius) in forward flight condition (Watkins et al. 2016).

So far, charge-coupled device (CCD) image sensors are used for single-shot lifetime measurements. As known from particle-image velocimetry (PIV) applications, the use of interline transfer CCD sensors enables the acquisition of two images in fast succession. The corresponding image readout scheme is also known as double-shutter mode. However, in state-of-the-art scientific grade CCD cameras the second exposure is several milliseconds long. The resulting image is therefore susceptible to blur due to the captured luminescence being emitted by the moving blade. In this case, the extent of blur depends on the rotating speed of the blade and the lifetime of the dye employed. Juliano et al. (2011) used a paint with a limited lifetime to reduce blur yet compromised signal intensity and the principal ability for applications on non-axisymmetric flows (Juliano et al. 2012), where fast-responding paints (see Gregory et al. 2014b) are preferred. It appears obvious, that any blur of this kind leads to a faulty recovered pressure signal. Gregory et al. (2014a) demonstrated the resulting under- and over-estimation of pressure at the blade leading- and trailing-edges, respectively.

1.3 Blur elimination techniques

Up to now, two principles exist countering the problem of rotational image blur in aerodynamic testing. On the one hand, Juliano et al. (2012) presented an image de-blurring algorithm, which was further developed by Gregory et al. (2014a). It employs a spatially invariant point spread function (PSF) based on the rotation rate of the blade and the luminescent lifetime of the PSP. Because the latter depends on the pressures to be solved for, the method biases regions exhibiting large pressure gradients. Additionally, the routine amplifies noise inherent to the raw images and introduces

artificial ringing patterns (“Gibbs ringing”) in regions with sharp contrast levels debasing the quality of the final results especially near the blade trailing edge (Gregory et al. 2014a; Watkins et al. 2016). On the other hand, Raffel and Heineck (2014) demonstrated a technique to mechanically de-rotate images using a rotating mirror setup for image acquisition. It is useful in applications where low signal levels are expected as it allows to increase the exposure time significantly (Lang et al. 2015). However, good optical access and sufficient space are required. If the rotor is tested in propeller configuration, the mirror has to be installed preferably in “off-axis” configuration (Raffel et al. 2017) causing additional challenges in order to synchronize the rotation rates of the mirror setup and the rotor. Both methods have recently been compared in more detail by Pandey et al. (2016).

1.4 Paper contribution

This work presents an optimized image acquisition technique dedicated to solve the problem of image blur in single-shot PSP lifetime measurements on fast rotating blades. After presenting the working principle and the characteristics of the measurement system employed, its capability to efficiently reduce blur is demonstrated. The system is then applied to measure surface pressures on the suction side of a Mach-scaled helicopter blade in climb. Following a description of the experimental setup, the post-processing procedures are presented, including measures to correct for temperature effects in the PSP data. Surface pressure results are then presented for different rotating speeds and various collective pitch settings before the measurement uncertainty is assessed.

2 Measurement system

The measurement system components used in this work are sketched as a principle test setup in Fig. 1.

The pressure-sensitive paint employed is platinum tetra(pentafluorophenyl) porphyrin (PtTFPP, Puklin et al. 2000) embedded in a poly(4-*tert*-butylstyrene) polymer binder [poly(4-TBS), see Yorita et al. 2017]. A laser system consisting of four neodymium-doped yttrium–aluminum–garnet (Nd:YAG) lasers (*Quantel, BigSky CFR-400*) is used to excite the dye at a wave length of 532 nm (Puklin et al. 2000). The key component of the measurement system is a modified version of the scientific grade digital CCD camera *FoxCam4M* recently presented by Geisler (2014, 2017a) and now further developed for single-shot PSP lifetime applications on fast rotating blades. For synchronization of camera and light source with the PSP-coated rotor blade, a commercially available and programmable pulse

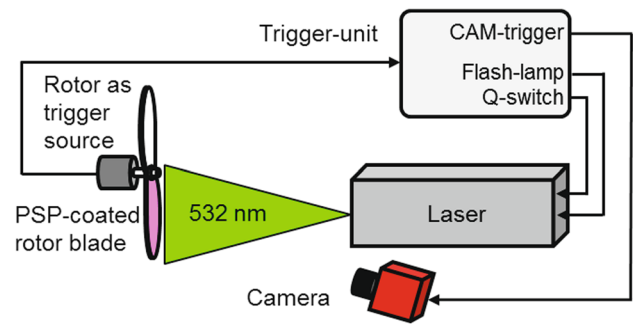


Fig. 1 Sketch of PSP-lifetime system components

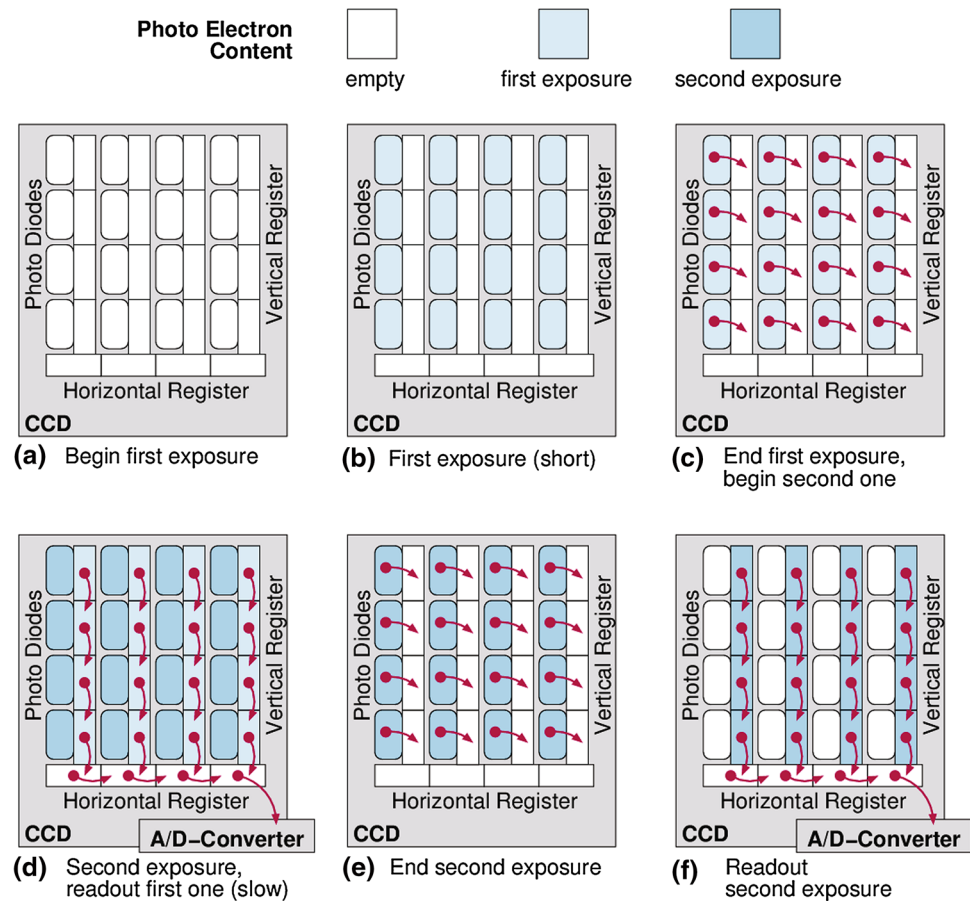
sequence generator (*Hardsoft, SequencerV5.1*) is used as triggering unit.

2.1 Image acquisition with *FoxCam4M*

The recording of two (or more) short-exposure frames in fast succession is limited by the technology of available image sensors. In this regard, the use of high-speed complementary metal-oxide semiconductor (CMOS) sensors reveals potential. For instance, Mebarki and Benmeddour (2016) applied a scientific CMOS camera for single-shot lifetime measurements on a slowly moving model. For the present application, however, exposure times below 10 μ s are required being equivalent to a recording rate of more than 100,000 fps. Today, image sensors reaching these frame rates provide only a limited spatial resolution. Similar requirements are known from flow measurements with particle-image velocimetry (PIV). For this, a new readout mode framing-optimized exposure (FOX) for off-the-shelf CCD image sensors was presented recently (Geisler 2014, 2017a). It provides two short exposed frames in fast succession. Both of them exhibit a binning-like reduced resolution and are completely congruent without insensitive lines or interlace-like artifacts. Because the second frame has a different exposure time for even and odd numbered pixel lines, the already presented readout mode is not suitable for luminescence lifetime measurements. For this purpose well-defined exposure times are required, whereas insensitive lines in principle are acceptable. Therefore, a different readout scheme is necessary.

The standard readout scheme for interline-CCD image sensors is depicted in Fig. 2. First, the photodiode content is cleared (Fig. 2a). The photodiodes then accumulate photoelectrons released by the incoming light (Fig. 2b). After the exposure time for the first frame the accumulated photoelectrons are transferred to the light-shielded vertical register (Fig. 2c). Subsequently, the register content is read out serially by one (or more) analogue-to-digital (A/D) converters (Fig. 2d). This is a slow process with a resolution-dependent

Fig. 2 CCD image sensor readout scheme in normal mode (a–d) and double-shutter mode (a–f)



duration in the millisecond range. Immediately after the transfer of the charges to the vertical register the photodiodes again start to accumulate photo-electrons. Once the readout process is completed, these new charges optionally can be transferred to the now empty vertical register (Fig. 2e) and read out (Fig. 2f). As a result, a second frame with an exposure time of at least the frame readout time is recorded in direct succession of the first frame. This two-frame readout scheme is commonly known as “double-shutter” mode.

The readout scheme used in the present measurements can overcome the disadvantageous long exposure time of the second frame in double-shutter mode. Here, only the charges of every second photodiode row are transferred to the vertical register after the exposure of the first frame (Fig. 3b), whereas the remaining photodiodes are ignored (crossed out in the sketch). Therefore half of the potential wells forming the vertical register cells remain still empty (Fig. 3c). The potential wells are shifted by one line (Fig. 3d), taking contained charges with them and thus the empty register cells are located next to the photodiodes used in the first frame. This process takes only several microseconds posing a lower limit to the exposure time of the second frame of $\sim 5 \mu\text{s}$. Hence, the newly accumulated charges of the very same photodiodes can be transferred to these empty register cells after

a very short exposure time for the second frame (Fig. 3e). The two frames are then stored in a line-interleaved pattern within the vertical register (Fig. 3f) and can be read out analogue to the common way (Fig. 2d, f). Finally, the frames are separated again from the line-interleaved pattern to single frames by software.

In summary, the two captured frames are completely congruent and have a well-defined short exposure time both of which are essential for lifetime imaging. The frames are exposed in direct succession with a very short (nanosecond range) frame transition time defined by the transfer process to the vertical register (Fig. 3b). Only half of the photodiode rows are used, i.e. every second image row is insensitive which bisects the effective image readout resolution. This modified readout scheme was programmed to the firmware of the 4 megapixel camera *FOXCAM4M* presented by Geisler (2017a). In general, it can be implemented in all cameras equipped with an image sensor whose even and odd pixel lines can be addressed separately. This requires at least an adapted firmware and/or eventually severe changes in the hardware. For the presented experiments, a commercial camera based on the *Kodak/ON Semiconductor KAI-4021* image sensor has been modified with in-house hardware adaptations including a separate firmware layer. More

Fig. 3 CCD image sensor read-out scheme in the luminescence lifetime imaging mode used for the present measurements

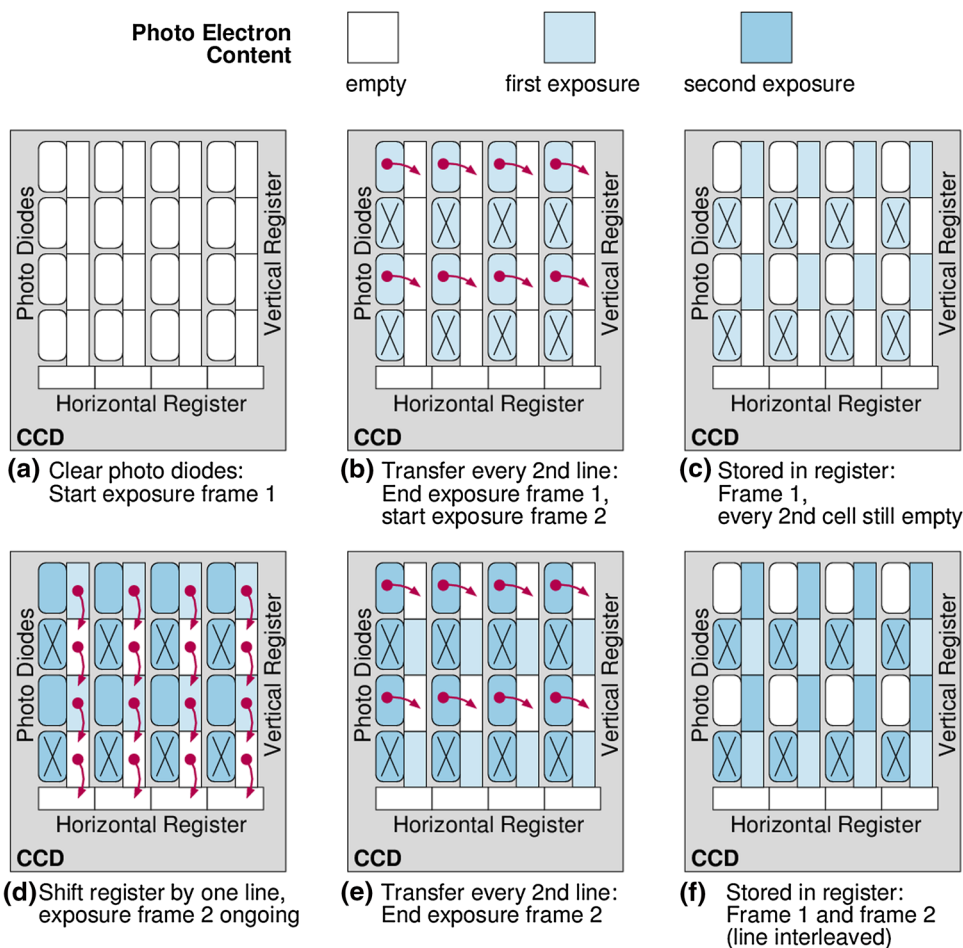


Table 1 Properties of *FoxCam4M* in lifetime mode

Sensor resolution	2048 × 2048 px
Effective readout resolution	2048 × 1024 px
Exposure time 1st frame ($G1$)	Customizable to $\geq 5 \mu\text{s}$ (typ.)
Exposure time 2nd frame ($G2$)	Customizable to $\geq 5 \mu\text{s}$ (min)
Frame transition time	<200 ns
Max. (double) frame rate	15 Hz
A/D dynamic range	12 bit

specific details are described by Geisler (2017b). The modified camera properties are given in Table 1.

A principle timing chart of the system components is provided in Fig. 4. Assuming that a trigger signal is provided by the rotor, a delay (preferably a phase shift) needs to be set with respect to the camera trigger in order to position the rotating blade in the camera field of view. The phase-shifted signal then triggers a sequence for both laser and camera. Considering the internal camera delay (set to $10 \mu\text{s}$) the parameter $\Delta t_{G1 \rightarrow \text{laser}}$ defines the timing between the excitation pulse and the beginning of the first exposure ($G1$). Here, positive values of $\Delta t_{G1 \rightarrow \text{laser}}$ cause the

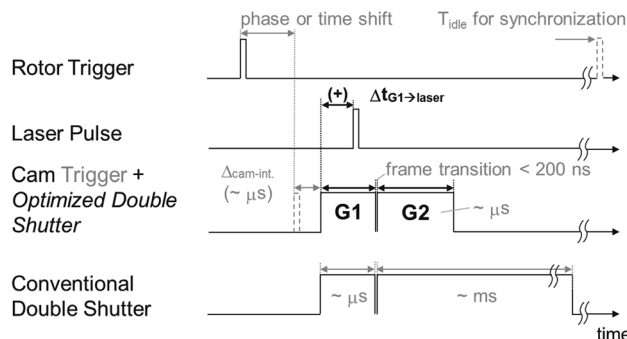


Fig. 4 Principle trigger sequence for optimized double-shutter PSP lifetime system applied to rotor testing

laser to pulse within the first frame. Because the pressure-sensitive signal immediately reacts to the excitation pulse, the key timing parameters determining the measured dye properties are the exposure lengths $G1$, $G2$ and $\Delta t_{G1 \rightarrow \text{laser}}$. If the data acquisition rate f_{acq} (limited by either laser or camera) is lower than the rotating frequency of the blades (f_{rotor}), an idle time (T_{idle}) needs to be implemented to the trigger sequence in order to synchronize the rotating speed

with laser and camera for phase-locked imaging. In the present study, the limiting system component is the laser. Being preferably pulsed at 10 Hz, T_{idle} was set to 95 ms.

2.2 Pressure-sensitive paint lifetime characteristics

The PSP employed here [PtTFPP in poly(4-TBS)] has been used previously for PSP-lifetime measurements on fast rotating blades by Klein et al. (2013). Being commonly excited by ultra-violet light emitting diodes, its characteristics were recently studied by Yorita et al. (2017). In the following, the pressure and temperature sensitivities are investigated for different settings of the timing parameters as outlined in Fig. 4 and considering dye excitation by a laser at 532 nm.

Therefore, a small coupon was prepared with the same coating layer setup as used in the wind tunnel test. A matte white foil (3M Wrap Film Series 1080, ~90 μm) is used as base layer to enhance the luminescent signal. Before applying the PSP an intermediate layer of boron nitride dissolved in the same polymer as the PSP is used (see also Yorita et al. 2017) to avoid any unwanted interactions between the active layer and the foil. A photo-multiplier tube (PMT) was used to measure the paint luminescence lifetime after pulsed excitation (10 Hz) at 532 nm by the laser mentioned above. A 650 ± 40 nm band-pass filter was used to separate the emitted light from the excitation pulse. The PMT signal was recorded by a digital oscilloscope at a sampling rate of 50 MHz for a total of 20 μs and ensemble averaged over 128 cycles. The sample was calibrated in a pressure- and temperature-controlled chamber. Lifetime decay curves were obtained for pressures from $p = 70\text{--}120$ kPa ($\Delta p = 10$ kPa) and for temperatures of $T = 15, 20$ and 25 °C, respectively. Selected decay curves are presented in Fig. 5, where all intensities are normalized by the peak value and plotted versus time. As expected, the decay rate is faster with both increasing pressure and temperature and the change in pressure has greater influence on the decay time within the depicted parameter range.

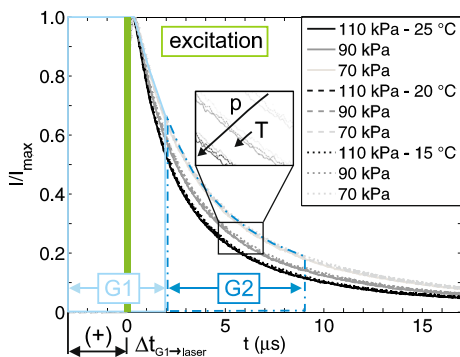


Fig. 5 Lifetime decay curves and schematic of integration gates $G1$ and $G2$ $\Delta t_{G1 \rightarrow laser}$ is positive when excitation is pulsed during $G1$

For further analysis the normalized intensity values are integrated over two adjacent gates, $G1$ and $G2$, as sketched in Fig. 5. The integration time $G1$ is chosen to be 5 μs and the timing parameters to be optimized are the delay between the start of $G1$ and the laser pulse, $\Delta t_{G1 \rightarrow laser}$, as well as the length of the second integration gate, $G2$. Note that the effective first exposure is reduced if the excitation light is pulsed within $G1$, i.e. for positive values of $\Delta t_{G1 \rightarrow laser}$. The ratio of the respective integrated intensities, $\frac{I_{G1}}{I_{G2}}$, is then normalized with the ratio at reference condition (100 kPa, 20 °C) and evaluated as ratio of ratios (RoR, see Eq. 1).

Pressure and temperature sensitivities s_p and s_T are defined as

$$s_p = \frac{\Delta RoR}{\Delta p} \times 100, \tag{2}$$

$$s_T = \frac{\Delta RoR}{\Delta T}. \tag{3}$$

The evaluated parameter range and the corresponding sensitivity results are summed up in Table 2. The following main conclusions can be drawn:

1. s_p increases with increasing $G2$,
2. s_p decreases for $\Delta t_{G1 \rightarrow laser} < 0$, i.e. start of $G1$ follows the excitation pulse,
3. Influence of $\Delta t_{G1 \rightarrow laser}$ on s_p is small for $\Delta t_{G1 \rightarrow laser} > 0$.

In view of a rotor test application, the length of $G2$ therefore has to be traded off between high-pressure sensitivity at long exposures and a small remaining extent of image blur at short exposure times. Moreover, it is desirable that the intensity levels of both gates are similar in order to reduce the effect of shot noise on the divided ratio image. This can be achieved by adopting $\Delta t_{G1 \rightarrow laser}$ accordingly, e.g., $\Delta t_{G1 \rightarrow laser} = +3$ μs for $G1|G2 = 5|7$ μs.

To confirm the PMT findings, the coupon was also calibrated using the *FoxCam4M* at exposure times of $G1|G2 = 5|7$ μs and a delay of $\Delta t_{G1 \rightarrow laser} = +3$ μs. In Fig. 6, the normalized gate ratio is plotted versus pressure for both

Table 2 Pressure and temperature sensitivities for different gate settings at 100 kPa, 20 °C

$G1 G2$ (μs)	$\Delta t_{G1 \rightarrow laser}$ (μs)	s_p (%/100 kPa)	s_T (%/K)
5 5	+3.0	56.7	0.34
5 7	+3.0	61.2	0.37
5 10	+3.0	66.8	0.39
5 7	+1.5	62.0	0.34
5 7	-1.5	38.7	0.18
5 7(<i>FoxCam4M</i>)	+3.0	55.3	0.40

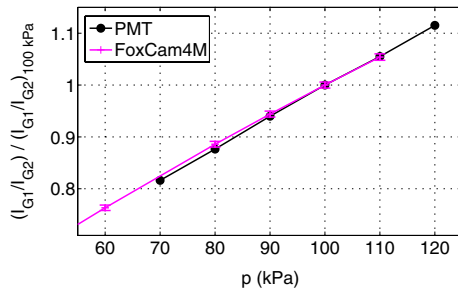


Fig. 6 Calibration results obtained by *FoxCam4M* vs. PMT data at $T = 20\text{ }^\circ\text{C}$; $G1|G2 = 5|7\text{ }\mu\text{s}$; $\Delta t_{G1 \rightarrow \text{laser}} = +3\text{ }\mu\text{s}$

the data obtained by the camera and the reference PMT measurements at $T = 20\text{ }^\circ\text{C}$. The error bars indicate the propagated measurement uncertainty averaging 128 images to obtain each of the four gate intensities used for the ratio of ratios calculation (Eq. 1). It can be deduced from the graph that the images recorded by the camera produce the expected results. Possible reasons for deviations include that the manner of integrating the luminescence signal differs between the analysis of PMT data and camera image acquisition.

2.3 Initial proof-of-concept

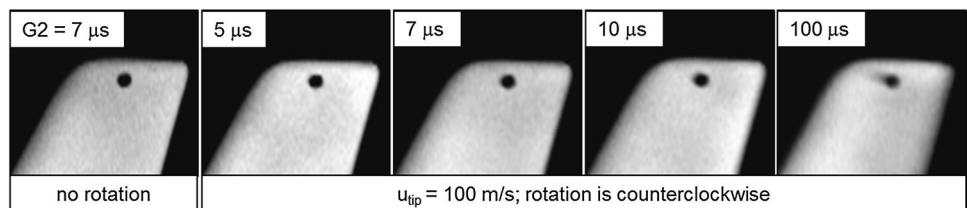
A laboratory study was conducted to demonstrate both system feasibility and the influence of different exposure times of the second gate on the blur of the resultant images. For this, a two-bladed, wooden model propeller (*EM-Elektro*) was used. It has an outer diameter of 0.35 m at 0.23 m pitch. Instead of the foil used for calibration, a white, acrylic-based screen layer (*Tamiya PS-1*) was applied on one of the blades before coating the same intermediate and PSP layers as described in the previous section. The test setup principally corresponds to the sketch in Fig. 1. The camera and light source were placed $\sim 4\text{ m}$ in front of the propeller in order to simulate larger wind tunnel facility dimensions. A Sonnar lens with a focal length of 180 mm and an aperture opening of $f/2.8$ provided images of the propeller blade at a chord-wise resolution of 4.6 px/mm for a tip chord length of 12 mm. Moreover, a $650 \pm 40\text{ nm}$ band-pass filter was used to separate the excitation light from the measured luminescence. Details about the propulsive unit and the $\frac{1}{\text{rev}}$ -trigger generation are described by Yorita et al. (2012) and Klein et al. (2013) who used a similar setup. The $\frac{1}{\text{rev}}$ -signal was

phase-shifted to position the blade within the camera image. The shifted signal was then directed into the triggering unit which generated a sequence as sketched in Fig. 4 to control the timing between camera and laser. The laser system was operated at 200 mJ/pulse and the rotation rate of the propeller was set to 90 Hz corresponding to tip-velocities of $\sim 100\text{ m/s}$. Choosing a $G1$ -exposure of $5\text{ }\mu\text{s}$ and a delay of $\Delta t_{G1 \rightarrow \text{laser}} = +1.5\text{ }\mu\text{s}$ the study was performed for $G2$ -lengths of 5, 7, 10 and $100\text{ }\mu\text{s}$. The latter was chosen to be fairly larger than the lifetime of the paint ($\tau_{0.1I_{\text{max}}} = 12\text{ }\mu\text{s}$ at 100 kPa, $20\text{ }^\circ\text{C}$) in order to simulate the second exposure of a conventional CCD-camera in double-shutter mode. The delay $\Delta t_{G1 \rightarrow \text{laser}}$ was chosen as an ‘‘appropriate guess’’ for approximately balanced image intensities between the first exposure ($G1 = 5\text{ }\mu\text{s}$) and the second exposures ($G2 = 5\text{--}100\text{ }\mu\text{s}$). Note from Table 2 that the effect of different positive delays on pressure sensitivity is small.

A series of the resulting $G2$ -exposures is presented in Fig. 7. Cut-outs of raw images are displayed showing particularly the blade tip. From the viewer’s perspective the rotational sense is counter-clockwise. In order to facilitate the visual perception of the resultant blur, a black round dot was painted close to the tip. The image on the left-hand side was acquired with the propeller at rest for $G2 = 7\text{ }\mu\text{s}$. It serves as a reference exhibiting a sharp contrast around the marker as well as alongside the blade edges. In contrast, the image simulating the second exposure of a conventional CCD double-shutter camera with $G2 = 100\text{ }\mu\text{s}$ is presented on the right-hand side of the figure. A dark trace appears in the vicinity of the marker in addition to the smoothed out blade edges. The pattern is similar to the blurred images recorded for instance by Gregory et al. (2014a).

Comparing the results for $G2 = 5, 7$ and $10\text{ }\mu\text{s}$ with $G2 = 100\text{ }\mu\text{s}$ the smear is reduced significantly which proves the capability of the *FoxCam4M* to acquire sharp $G2$ -images when applying the single-shot PSP-lifetime technique. Still, a residual but gradually increasing blur can be observed with increasing exposure time. The distance swept by the blade tip at $f_{\text{rotor}} = 90\text{ Hz}$ and $G2 = 7\text{ }\mu\text{s}$ is $\Delta x = 0.7\text{ mm}$ corresponding to 3.2 px or 5.8% chord in this case. It should be emphasized here, that using the optimized double-shutter technique of the *FoxCam4M*, image blur is inherently limited to only a few pixels for both successively acquired images (I_{G1}, I_{G2}). Therefore, presuming that the signal recorded during both gated exposures suffices the use of de-blurring

Fig. 7 Images of propeller tip from second exposure of optimized double-shutter mode for different exposure times $G2$. Colormap is centered to include 95% of existing count values, respectively



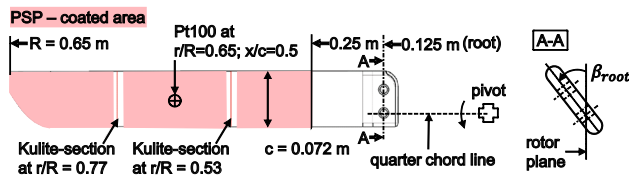


Fig. 8 DSA-9A rotor blade with SPP8 tip for PSP investigation and definition of root pitch angle β_{root} . Sketch is modified from Schwermer et al. (2016) and not to scale

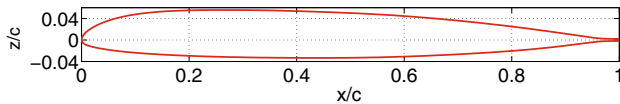


Fig. 9 Contour of tabbed DSA-9A airfoil, relative thickness is 9%

algorithms or image de-rotation techniques can be omitted. A resultant $G1$ -image is not shown here because the effective exposure is even shorter than $5 \mu s$ due to the delayed excitation pulse during $G1$, which results in even less residual blur as compared to $G2$.

To conclude, the choice of the optimum $G2$ -width should be short enough to limit image blur within an allowable maximum. Within the application-specific tolerance, a longer $G2$ is favorable as it provides both greater pressure sensitivity (see Sect. 2.2) and higher signal intensity. However, it should be considered that the intensity gain is not directly proportional to the second exposure time due to the lifetime decay (see Fig. 5).

3 Application to rotating helicopter blades in climb

3.1 Model and facility

The main experiment was conducted in the rotor test facility at the German Aerospace Center (DLR) in Göttingen developed by Schwermer et al. (2016, 2017). The investigated rotor is equipped with two blades made out of carbon fiber reinforced plastic. As indicated in Fig. 8, they have a tip radius of $R = 0.65 \text{ m}$ and a chord length of $c = 0.072 \text{ m}$. For $r > 0.16 \text{ m}$ the blades are equipped with the DSA-9A helicopter airfoil (Fig. 9) and the parabolic SPP8 tip without anhedral (Vuillet et al. 1989). A

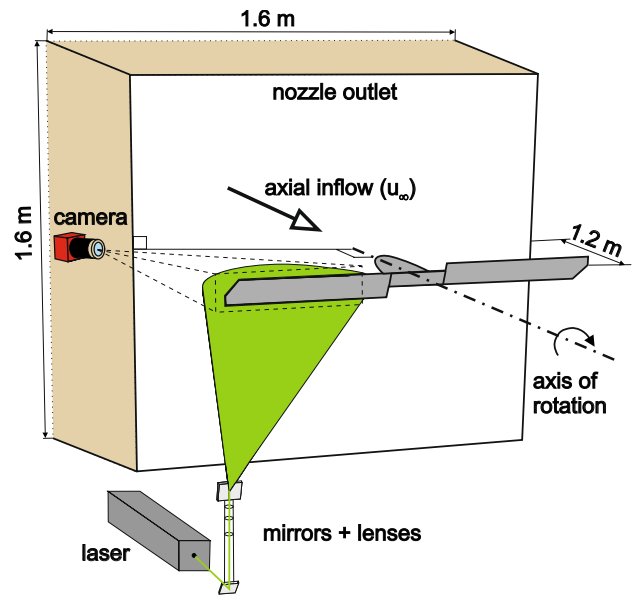


Fig. 10 Experimental setup in the rotor test facility of DLR Göttingen

negative linear twist of -9.33° is incorporated along the blade’s span between $0.16 \text{ m} < r < 0.65 \text{ m}$ with an offset of -0.67° between the blade root and $r = 0.16 \text{ m}$. In one of the blades fast response pressure transducers (Kulite LQ-062) are installed at the two relative radial positions, $\frac{r}{R} = 0.77$ and $\frac{r}{R} = 0.53$, respectively. The exact positioning of the sensors providing valid data on the blade suction side is listed in Table 3. Additionally, a Pt100-temperature probe is installed close to the surface of the PSP-blade suction-side at $\frac{r}{R} = 0.65$ and $\frac{x}{c} = 0.5$.

As illustrated in Fig. 10, the rotor is placed vertically in the open test section of the facility with the rotation plane facing the square nozzle outlet ($1.6 \text{ m} \times 1.6 \text{ m}$) at a distance of 1.2 m (i.e. $\sim 1.8 R$). The maximum allowable rotating speed is $f_{rotor,max} = 50 \text{ Hz}$. Moreover, a defined low-speed axial inflow of maximal $u_{\infty,max} = 14 \text{ m/s}$ can be provided by the Eiffel-type wind tunnel in order to avoid recirculation and blade vortex interactions. The test stand further allows for the adjustment of both the geometric collective and cyclic pitch angles at the blade root (β_{root} as defined in Fig. 8). Here, only the collective pitch was varied equally for both blades and the cyclic pitch was kept to a minimum of $0 \pm 0.05^\circ$ which is considered to be negligible. Therefore, the arrangement corresponds to a slowly advancing propeller or a helicopter rotor in climb.

Table 3 Relative radial (r/R)- and chord-wise (x/c) positions of available Kulite sensors on blade suction side

r/R	x/c					
0.77	0.028	0.110	0.194	0.310	0.620	0.806
0.53		0.110	0.194		0.620	

3.2 Measurement system installation

The laser was installed underneath the wind tunnel nozzle as depicted in Fig. 10. An arrangement of mirrors and lenses below the nozzle outlet redirected the beam towards the rotor in the form of an elliptic spot to ensure full illumination of the coated area. The distance between the optical setup and the illuminated blade was approximately 1.5 m. In order to maximize the paint luminescent signal the quadruple laser system was operated at a nominal power of 800 mJ/pulse (4×200 mJ/pulse). The *FoxCam4M* was mounted next to the nozzle outlet at the height of the rotor hub. A 35-mm *Nikkor* lens was installed under *Scheimpflug* condition (Bickel et al. 1985) to achieve sharp images across the coated span of the blade (see Figs. 10, 11). With this setup, the final spatial resolution is 2.6–3.3 px/mm in chord-wise direction with higher values at the blade tip. The blade being instrumented with Kulites was coated with the PSP as described in Sect. 2.2, and the pressure transducer rows were masked before the coating was applied. An image of the installed and PSP-coated blade is provided in Fig. 11 on the right-hand side.

Considering the lifetime parameter study of the PSP in view of the configuration investigated, a setting of $G1|G2 = 5|7 \mu\text{s}$ and $\Delta t_{G1 \rightarrow \text{laser}} = +3 \mu\text{s}$ (see Table 2, Sect. 2.2) was selected in order to get sharp images at high-pressure sensitivity and balanced intensity levels between both frames. At a maximum blade tip speed of $u_{\text{tip}} = 193$ m/s ($f_{\text{rotor}} = 47.2$ Hz) the resulting blur pattern for $G2 = 7 \mu\text{s}$ is 1.3 mm at the tip corresponding to 1.8% chord and 4.4 px. Calibration was conducted using the same measurement system as in the test obtaining pressure and temperature sensitivities of 55.3%/100 kPa and 0.40%/K under reference conditions (100 kPa, 20 °C), respectively.

3.3 Data acquisition

In the setup described, an encoder was mounted to the rotating shaft providing a $\frac{1}{\text{rev.}}$ and a $\frac{1000}{\text{rev.}}$ TTL-signal. A custom-made “selective-trigger-box” then allowed to position the rotating blade within the camera field of view as sketched in Fig. 10. The positioning was done by selecting the appropriate rising edge of the encoder signal and feeding the properly shifted $\frac{1}{\text{rev.}}$ -signal as trigger input to the sequencer, which generated the synchronized signals for laser and camera

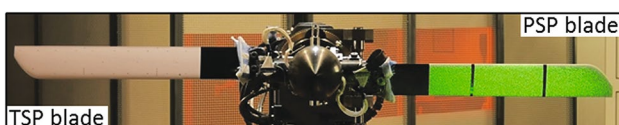


Fig. 11 PSP- and TSP-coated rotor blades in rotor test facility of DLR Göttingen. PSP-blade is illuminated by laser light at 532 nm

according to Fig. 4 using the settings as listed for the *FoxCam4M* in Table 2.

Initially, dark-images were acquired under the absence of excitation light and at minimum background illumination. As the rotor was at rest, the blades were set to reference position as sketched in Fig. 10 for the acquisition of wind-off images. Considering that the blade surface temperature reaches an asymptotic value after adjusting for the desired rotating speed, the time signal of the temperature probe on the suction side of the PSP-blade was monitored online to ensure data acquisition under equilibrium condition. In practice, the rotor was running for ~ 90 s until an asymptotic value was reached and the image acquisition process was started under wind-on condition.

For each data point a series of 128 double frames, i.e. pairs of $G1$ and $G2$ images, was acquired in order to increase the SNR by ensemble averaging the respective single-shot results. Depending on $f_{\text{rotor}} = 23.6, 35.4$ and 47.2 Hz, the image acquisition rate was limited to every third, fourth or fifth revolution, resulting in acquisition rates of $f_{\text{acq.}} = 7.9, 8.9$ and 9.4 double frames per second (fps), respectively.

Kulite and Pt100 data are provided at a bandwidth of 19 kHz and balance readings are sampled at 200 kHz. All rotor data were averaged over a period of 10 s. More detailed information about the rotor data acquisition system is provided by Schwermer et al. (2017).

4 Data processing

4.1 Data reduction

After the images were read out, a 2×1 binning was applied. This way, the SNR is increased by $\sqrt{2}$ and the original image aspect ratio is recovered (Sect. 2.1). All image processing is then performed using the in-house developed software package *ToPas* (as in Klein et al. 2005) according to the following procedure:

1. Dark signal subtraction from all images,
2. 2D-image registration: all images acquired under wind-on condition are aligned to the first $G1$ image of the series using 23 dot-markers applied to the coated surface; the procedure accounts for rotation and translation within the image plane,
3. Wind-off ratio: ensemble averaging of 128 double frames and calculation of $\bar{R}_{\text{wind-off}} = \left(\frac{I_{G1}}{I_{G2}} \right)_{\text{wind-off}}$,
4. Wind-on ratio: for single-shot result only a single double frame is considered for $R_{\text{wind-on}} = \left(\frac{I_{G1}}{I_{G2}} \right)_{\text{wind-on}}$; for ensemble-averaged results the mean of all 128 wind-on ratios is calculated $\left(\bar{R}_{\text{wind-on}} \right)$,

5. 3D-image projection of wind-off and wind-on ratio images to blade surface grid with a resolution of 0.9–1.1 nodes/px; the projected image is 5×5 median filtered before mapping is applied,
6. Ratio of ratios calculation according to Eq. (1),
7. Application of calibration polynomial (Eq. 1) under consideration of temperatures at each node (see Sect. 4.2),
8. Application of offset correction according to Sect. 4.3.

A single-shot pressure result obtained at a rotation rate of $f_{\text{rotor}} = 35.4$ Hz and a collective pitch of $\beta_{\text{root}} = 17^\circ$ is presented in Fig. 12. For the results presented, a homogeneous temperature distribution based on the probe reading underneath the blade surface at $r/R = 0.65$ is assumed at step 7 of the above-mentioned data reduction procedure. Principal features of an expected pressure distribution can be assessed. A low-pressure region corresponding to stronger suction evolves along the leading edge followed by a pressure increase towards the trailing edge. Close to the blade tip, at $r/R \sim 0.99$, a small region of relatively low pressures is visible denoting the footprint of the tip vortex.

4.2 Temperature correction

The surface temperature on a rotating blade was previously approximated by the adiabatic wall recovery temperature (Disotell et al. 2014; Watkins et al. 2016). It can be expressed as

$$T_{\text{ad.wall}} = T_\infty + r(Pr) \frac{\kappa - 1}{2} \frac{V_{\text{rot}}^2}{\kappa R_{\text{air}}}, \quad (4)$$

where T_∞ is the free stream temperature, $r(Pr)$ is the recovery factor as a function of the Prandtl number and κ and R_{air} are the ratio of specific heats and the gas constant for air. Due to the linear dependency of the resulting velocity at the respective blade radius ($V_{\text{rot}} \propto f_{\text{rotor}} \cdot r$), the theoretical wall temperature increases quadratically from rotor hub to tip. Applying the values in Eq. (4) as proposed by Disotell et al. (2014) the estimated maximal radial temperature variation within the coated blade area is $\Delta T = 13.4$ °C at

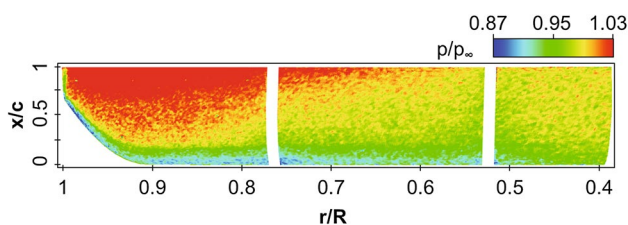


Fig. 12 Pressure result of temperature uncorrected single-shot ratio of ratios at $f_{\text{rotor}} = 35.4$ Hz; $\beta_{\text{root}} = 17^\circ$. Rotation is counter-clockwise

$f_{\text{rotor,max}} = 47.2$ Hz. The resulting error in pressure would be $\Delta p \sim 9.7$ kPa if the pressure and temperature sensitivities of 55.3% /100 kPa and 0.40%/K (see Table 2) are considered.

To account for this effect, a temperature map is approximated by calculating a value for $T_{\text{ad.wall}}$ for each node on the 3D grid according to its radial position and resulting rotational speed (Eq. 4). T_∞ is obtained by assuming that the temperature probe on the PSP-blade suction side provides the value of $T_{\text{ad.wall}}$ at $r/R = 0.65$ and $x/c = 0.5$. This way, the approximated temperature map is “anchored” at the position of the associated temperature measurement on the PSP-blade. Because the temperature sensor is applied just underneath the original blade surface, the reading might differ from the actual temperature of the PSP-coating at that position due to the foil between the coating and the blade surface. Nevertheless, an offset in T_∞ can be accounted for (see Sect. 4.3) and does not affect the radial distribution according to Eq. (4).

The validity of this approach is checked by measuring the temperature distribution on the second, structurally identical blade using a TSP coating (Fig. 11). For this purpose, PtTFPP was embedded inside the oxygen-impermeable polyurethane (PU) binder material (*Clearcoat, ANAC advanced coatings*) as it was previously done by Klein et al. (2013). Application of the same dye as for the PSP allows to use the identical optical setup additionally enabling efficient excitation at 532 nm. Before coating the TSP, the same white foil as used on the structurally identical PSP-blade is applied to ensure as similar boundary conditions as possible. The gate exposures are identical to the ones applied for the PSP-blade ($G1|G2 = 5|7 \mu\text{s}$). A delay of $\Delta t_{G1 \rightarrow \text{laser}} = -10.9 \mu\text{s}$ results in a temperature sensitivity of 0.2%/K. The residual pressure sensitivity of 3.5%/100 kPa was neglected and hence the calibration coefficients in the pressure terms of Eq. (1) are not considered for the evaluation of temperature. Besides that, the node-wise temperatures are deduced as described above in Sect. 4.1 (steps 1–6). An additional 7×7 median filter was applied at the end to smooth out residual spatial non-uniformities in the data.

The approximated temperature map and the temperatures measured by TSP are displayed in Fig. 13a, b, respectively. The results correspond to the conditions already presented in Fig. 12. In general, the temperatures measured by TSP resemble a radial temperature increase, as expected. Moreover, the measured temperature distribution appears to be rather two-dimensional for the most part of the surface, i.e. between $0.4 < r/R < 0.85$ and $0.1 < x/c < 0.85$. In this region, it is resembled particularly well by the theoretical approximation.

Detailed analysis of the TSP results reveal temperatures higher than the theoretical stagnation point temperature

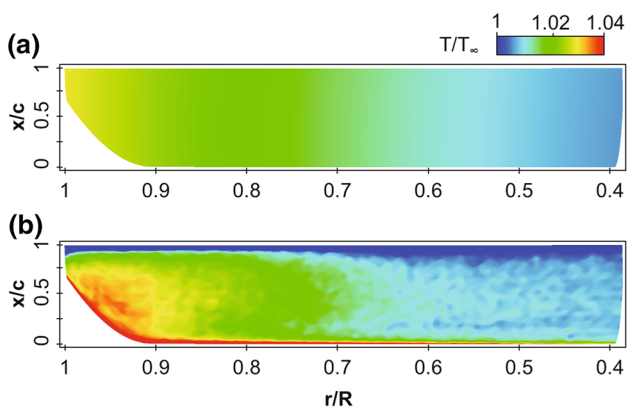


Fig. 13 **a** Approximated adiabatic wall temperature. **b** Temperatures measured by TSP. Same conditions as in Fig. 12

along the leading edge ($x/c < 5\%$) and values lower than the free stream temperature along the trailing edge ($x/c > 85\%$). These unphysical findings can neither be explained by faulty alignment or 3D-mapping nor by blurred images since both the applied post-processing and the image exposure times are identical for the PSP results (Fig. 12). Note also that any faulty trends due to image blur would be in the opposite direction (Gregory et al. 2014a). In fact, it is believed that the observed deficiencies result from unforeseen properties of the paint which was thinned out along the rounded leading edge and accumulated along the tabbed trailing edge (Fig. 9) during the drying process. As opposed to the PSP being sprayed onto an intermediate boron nitride layer, the TSP was directly applied on the foil probably causing different adhesive properties. At $r/R > 0.85$ the measured temperatures exceed the approximation up to a maximum delta of ~ 2.5 K for $x/c < 0.75$ and a 3D structure becomes visible the reason of which could not finally be assessed.

For these reasons, the adiabatic wall recovery temperature is further considered for correction purposes. The temperature-corrected single-shot result from Fig. 12 is presented in Fig. 14. As opposed to the uncorrected pressure map, the radial pressure gradient is reduced, as expected.

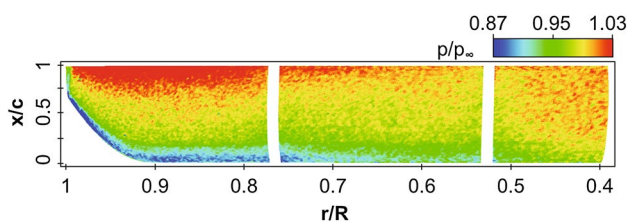


Fig. 14 Single-shot pressure result of Fig. 12 after temperature correction with adiabatic wall temperature from Fig. 13a

4.3 Offset correction

In PSP measurements any uncertainty in the bulk temperature level of the model surface between wind-off and wind-on condition causes a bias in the final result. Therefore, if pressure tap data are available, it is common practice to correct for this offset by “anchoring” the PSP-data using the available tap readings nearby (McLachlan and Bell 1995). Unfortunately, it is observed in this study, that the Kulites installed in the PSP-coated blade pose an internal heat source to the dye which causes a bias in the vicinity of the respective transducer sections due to the temperature sensitivity of the PSP. Note that this bias can neither be corrected by the approximated wall recovery temperature, nor by the temperature measured on the second blade since this is not instrumented with pressure sensors.

During the measurement campaign, the data point presented above was repeated with Kulites switched off. The difference of the ensemble-averaged results between the “Kulite-on” and “Kulite-off” condition ($p_{\text{Ku-on}} - p_{\text{Ku-off}}$) is displayed in Fig. 15. It can be deduced that the pressure is underestimated by more than 1 kPa close to the pressure tap sections when the transducers are powered. As opposed to the wind-off condition, part of the excess heat from the Kulites is convected by the free stream under wind-on condition. This leads to relatively lower values of $\frac{T_{\text{wind-on}}}{T_{\text{wind-off}}}$ and therefore relatively lower pressures as compared to the Ku_{off} condition (see Eq. 1). The observed pressure delta of up to 1 kPa is therefore attributed to underestimated temperatures in the range of 1.25–2 K assuming the corresponding sensitivities at pressures between 100 and 70 kPa.

A general estimation of the resulting temperature on the surface influenced by the Kulite heating is complex. Therefore, the following method is applied in order to correct for an offset in the PSP-data and to compare available pressure tap measurements to PSP-data not influenced by the effect shown. In Fig. 15, circles indicate the Kulite locations where data are available at same chord-wise positions for both radial sections, respectively. The PSP-data in between, marked as crosses at $r/R = 0.65$ in Fig. 15, is now compared

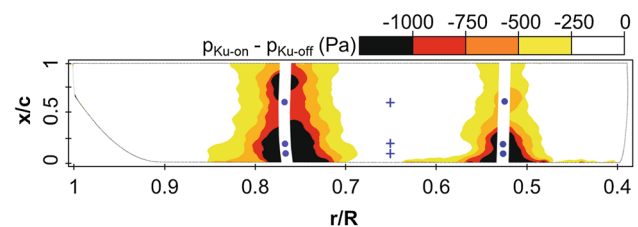


Fig. 15 Pressure error caused by internal heating of Kulites for conditions presented in Fig. 12. Circles and crosses indicate positions of Kulite and PSP data used for offset correction

to the mean of the adjacent pressure tap measurements at the same chord-wise locations according to Eq. (5).

$$\Delta_{\text{offset}} = \frac{1}{3} \sum \left[p_{\text{PSP},0.65R,\frac{x}{c}} - \left(\frac{p_{\text{Ku},0.77R} + p_{\text{Ku},0.53R}}{2} \right)_{\frac{x}{c}} \right];$$

$$\frac{x}{c} = 0.11; 0.19; 0.62. \quad (5)$$

The deduced value describes the average delta between the mean of the corresponding Kulite readings at the same chord-wise positions of both radial sections and the respective PSP-value in between. During post-processing Δ_{offset} is added as a bulk shift to all values on the 3D-grid. In this campaign the magnitude of the applied offset was in the order of 300 Pa. Note that the correction method implies a linear development of pressure between $0.53 < r/R < 0.77$, which cannot be physically justified. Therefore, this approach is regarded as best practice here.

As the final post-processing step, the “delta-pressures” presented in Fig. 15 are subtracted from the offset-corrected results in order to account for the Kulite heating effect. This is only an approximate correction for other data points at different pitch settings and especially at different rotating speeds as the effect is influenced by the convective heat transport from the surface. Therefore, a quantitative discussion of the PSP-data in the vicinity of the Kulite sections is omitted in the discussion of the results. To overcome these deficiencies in future experiments, it should be attempted to either measure the temperature of the PSP-coating directly or to repeat all data points with Kulites switched off.

5 Results and discussion

In Sect. 5.1, the surface pressure distribution is investigated at constant collective pitch for a variation of rotating speeds. The axial inflow velocity u_{∞} was adjusted proportionally to the rotating frequency in order to maintain a constant advance ratio J ($J = \frac{u_{\infty}}{2\pi f_{\text{rotor}} R}$). Furthermore, in Sect. 5.2, different blade loadings are examined at a constant rotation rate by variation of the collective pitch angle at $f_{\text{rotor}} = 23.6$ Hz. Here, indications of stalled flow are found and further investigated in Sect. 5.3. A summary of the investigated test conditions and the resulting blade tip Mach and chord Reynolds numbers (M_{tip} , Re_{tip}) are presented in Table 4.

5.1 Variation of rotating frequency

In Fig. 16, the surface pressure distribution is presented for rotating frequencies of $f_{\text{rotor}} = 23.6, 35.4, 47.2$ Hz at a collective root pitch angle of $\beta_{\text{root}} = 17^\circ$. The results displayed

Table 4 Test conditions

f_{rotor} (Hz)	23.6	35.4	47.2
M_{tip}	0.29	0.43	0.57
Re_{tip}	4.63×10^5	6.94×10^5	9.26×10^5
β_{root}	10° – 28°	17°	17°
$J = u_{\infty} / (2\pi f_{\text{rotor}} R) = 0.021 \pm 0.001$			

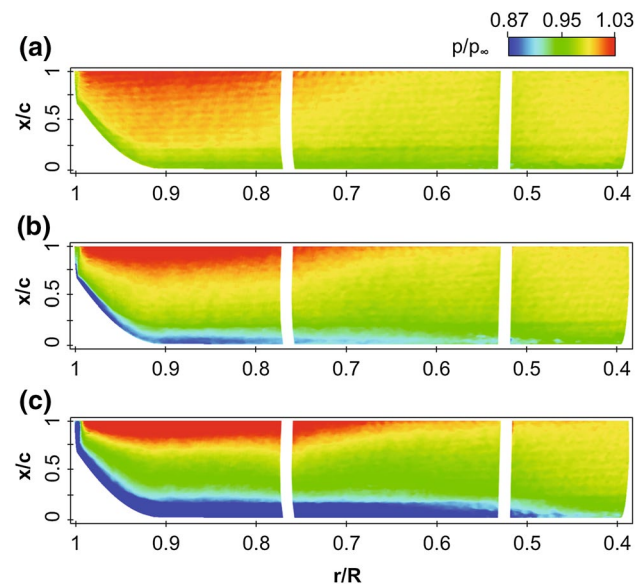


Fig. 16 Surface pressure distribution at $\beta_{\text{root}} = 17^\circ$ for different rotating frequencies $f_{\text{rotor}} =$ **a** 23.6Hz, **b** 35.4Hz, **c** 47.2Hz

are normalized by the ambient pressure and the same color map is used for all cases to ease a comparative discussion. Note the improved SNR due to ensemble averaging as compared to the single-shot result presented in Fig. 14. In all pressure maps shown, suction areas can be distinguished parallel to the leading edge and along the parabolic shaped blade tip followed by the expected pressure recovery in chord-wise direction. A comparison of the results reveals that the stream-wise pressure gradients are more pronounced as the rotating frequency is increased. This results in comparatively lower pressures close to the leading edge. The bigger suction effect at greater rotating frequencies is also manifested in the evolution of the footprint of the tip vortex. It appears as a low-pressure region with pronounced radial gradients near the blade tip. Note that the resulting surface pressure in this region decreases with increasing rotation rates. In view of the Kutta–Joukowski theorem the trend is plausible as the tip vortex is expected to gain strength (in terms of circulation) at higher blade velocities (Mahalingam et al. 2000) and thus induces higher velocities at the blade tip.

Note the visible horizontal stripe artifacts in Fig. 16. This phenomenon results from a sensor-specific fixed periodicity in the electrodes and exists both in horizontal and vertical direction. Since the periodicity is known (in the present case: 16 pixel vertically causing the horizontal stripes and 4 pixel perpendicular to that) appropriate spatial filters can be used to suppress the visibility of this effect (see e.g., Disotell et al. 2014). In the present case, the applied 5×5 median filter was sufficient to filter out the 4 pixel periodicity. The remaining horizontal stripes could not be filtered out efficiently by a spectral filter possibly due to the low number of stripes. Furthermore, aerodynamic structures exist (discussed below) with only slightly different orientation. As they could be affected by spectral filtering, the application of such a filter was omitted in this direction. Note from Fig. 16 that the described effect is predominant in the case of $f_{\text{rotor}} = 23.6$ Hz, and it is mostly obscured in the cases with higher SNR, i.e. at $f_{\text{rotor}} = 35.4$ and 47.2 Hz.

For further analysis, the chord-wise pressure distribution is extracted at $r/R = 0.65$ and plotted as p/p_∞ versus x/c in Fig. 17. Note the reversed vertical axis expressing increased suction at higher rotating frequencies. For all cases presented, a suction peak is distinguishable followed by a pressure increase towards the trailing edge as mentioned above. When plotted as p/p_∞ , the pressure levels and gradients principally scale with the resulting dynamic pressure which is a function of both radius and rotating frequency. Still, the pressure distribution also depends on the effective angle of attack at the respective cross-section. Since the advance ratio is reasonably constant for all f_{rotor} shown, the variation in angle of attack for the various

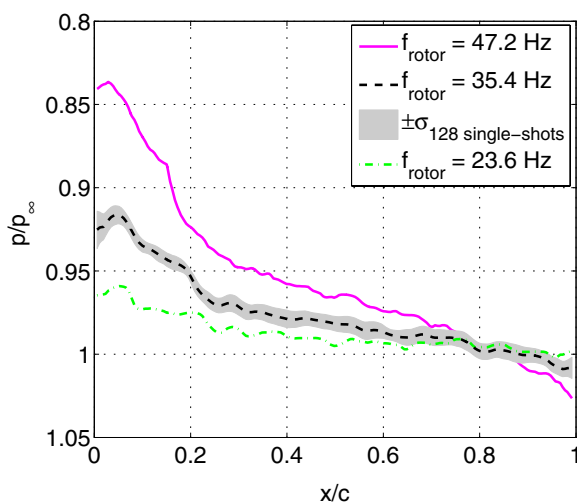


Fig. 17 Chord-wise pressure distribution extracted at $r/R = 0.65$ for different rotating frequencies at $\beta_{\text{root}} = 17^\circ$ (same cases as in Fig. 16). The shaded region denotes the standard deviation of 128 consecutive single-shot results

rotational speeds at $r/R = 0.65$ is expected to be small and the different pressure levels can mainly be attributed to the variation of dynamic pressure.

The data point corresponding to $f_{\text{rotor}} = 35.4$ Hz and $\beta_{\text{root}} = 17^\circ$ has been repeated four times. In Fig. 18, an average of the ensemble-averaged PSP-data of the four runs is plotted in terms of c_p based on the rotating speed at the respective radial section:

$$c_p = \frac{p - p_\infty}{\frac{\rho}{2}(2\pi f_{\text{rotor}} r)^2} \quad (6)$$

The shaded band includes the ensemble-averaged results of all repetitions and comprises $\Delta c_p < 0.15$ for the most part of the chord, which corresponds to ± 400 Pa in this case. Comparatively greater variations can be deduced close to the leading edge where the pressure distribution is sensitive to variations of the respective inflow conditions between the individual runs. For comparison, the available Kulite data are added to the graph. The symbols mark the mean of the four averages over the respective 10 s time series. Deviations of this mean are smaller than the symbol size. The bars indicate the pressure fluctuation in terms of the respective standard deviations σ_{c_p} averaged over the four runs. Note that the bar sizes are emphasized by multiplying the measured values times five. The Kulite readings at $r/R = 0.53$ exhibit slightly but consistently lower mean values in c_p than at $r/R = 0.77$ indicating a slightly lower effective angle of attack further outboard. The trend seems reasonable when considering the negatively twisted blade geometry and the expected increasing induced velocity by the tip vortex at higher radii.

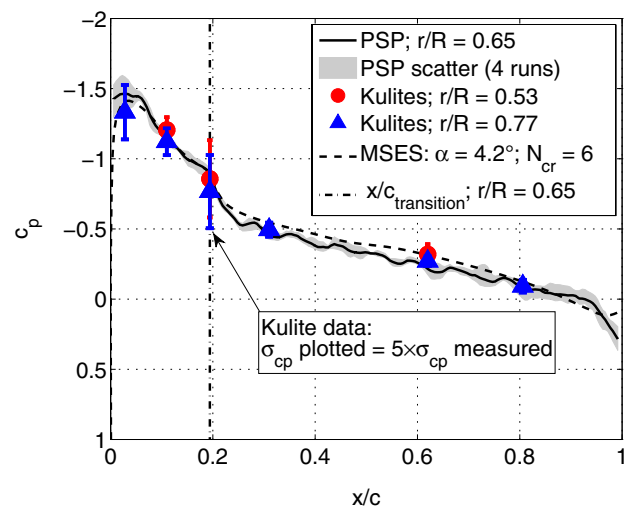


Fig. 18 Ensemble-averaged PSP and Kulite data from four repeated data points at $f_{\text{rotor}} = 35.4$ Hz, $\beta_{\text{root}} = 17^\circ$. MSES data correspond to conditions at $r/R = 0.65$ and $f_{\text{rotor}} = 35.4$ Hz. Vertical line indicates transition position detected from result in Fig. 19

Qualitatively, the PSP data resemble the trend prescribed by pressure transducers quite well. For this reason, it is assumed that the pressure distribution is quasi-two-dimensional between the pressure-transducer sections. This finding legitimizes the offset correction approach (Eq. 5) a posteriori.

An interesting aspect can be observed in the cross-sectional PSP-data for $f_{\text{rotor}} = 35.4$ and 47.2 Hz in Fig. 17 and for $f_{\text{rotor}} = 35.4$ Hz in Fig. 18. In both plots, the chord-wise pressure gradients exhibit an abrupt increase at $x/c \sim 0.19$ (at $f_{\text{rotor}} = 35.4$ Hz) and at $x/c \sim 0.15$ (at $f_{\text{rotor}} = 47.2$ Hz), respectively. In Fig. 18 the kink in the pressure distribution coincides with the maximum in σ_{c_p} indicating boundary-layer transition (Gardner and Richter 2015). However, in view of the sparse spatial resolution of pressure transducers the absolute maximum in σ_{c_p} might not be resolved and it is rather coincidental that the pressure discontinuity corresponds to the $\sigma_{c_p, \text{max}}$ -location from the available sensors.

Still, the observed discontinuity in the PSP-data can be explained by the laminar–turbulent boundary-layer (BL) transition phenomenon (see Popov et al. 2008).

To prove this, BL transition was measured in a separate test by means of TSP (Fey and Egami 2007) for the data point at $f_{\text{rotor}} = 35$ Hz and $\beta_{\text{root}} = 17^\circ$. The TSP coating and hardware employed as well as the post-processing steps are detailed by Yorita et al. (2012) and Lang et al. (2015). The result is presented in Fig. 19, where the displayed gray scale values of the TSP intensity ratio are a measure of the temperature on the heated model surface. Dark areas correspond to turbulent flow regions and lower surface temperatures due to more efficient cooling as compared to bright areas, which correspond to laminar or laminar separated regions (see Lang et al. 2015). It can be deduced from Fig. 19 that the transition region evolves nearly parallel to the leading edge, which supports the above-stated hypothesis of a predominantly two-dimensional pressure distribution across the blade. The transition position $(x/c)_{\text{transition}}$ is defined here as the chord-wise location of the maximum intensity gradient in the thermographic result corresponding to the location of 50% turbulence intermittency (Kreplin and Höhler 1992; Ashill et al. 1996). The transition position detected at

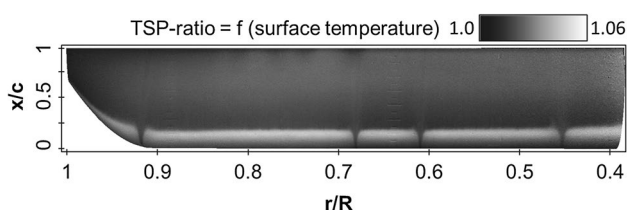


Fig. 19 Transition result from separate TSP experiment at $f_{\text{rotor}} = 35.4$ Hz, $\beta_{\text{root}} = 17^\circ$. Dark areas correspond to turbulent-, bright areas to laminar- or laminar separated flow regions. Turbulators are applied at four radial positions causing turbulent wedges further downstream

$r/R = 0.65$ is indicated by the vertical line in Fig. 18. It is particularly remarkable how well it coincides with the above-mentioned pressure discontinuity measured by PSP and the location of the Kulites exhibiting maximum values for σ_{c_p} . It should be mentioned that the observed discontinuity in the PSP data (in Fig. 18) partially originates from the different adiabatic wall recovery temperatures between laminar and turbulent boundary layers. Considering $T_\infty = 283$ K, $M_{0.77R} = 0.33$ and the recovery factors of \sqrt{Pr} and $\sqrt{Pr^3}$ for laminar and turbulent boundary layers (see Eckert 1962) at a Prandtl number of $Pr = 0.72$ for air, this temperature difference is ~ 0.3 K (according to Eq. 4). However, the “kink” in Fig. 18 is in the order of $\Delta c_p \sim 0.2$ corresponding to $\Delta p \sim 1500$ Pa. If pressure and temperature sensitivities at reference conditions (see Table 2) are taken into account, a temperature change of ~ 2.1 K would be necessary if the observed pattern was due to different temperatures only. Hence, the influence of chord-wise temperature differences between laminar and turbulent flow in the PSP results is assumed to be small and the observed discontinuity can mainly be attributed to a change in pressure. In contrast, the temperature differences in the TSP result of the same case (displayed qualitatively in Fig. 19) are amplified by heating the blade and reflect the differences in heat transfer between laminar and turbulent boundary layers. To conclude, PSP can in principle detect BL transition by the pressure gradient (for particular cases) when no other measurement technique is available.

In order to complement the experimental results, computations were performed using the coupled 2D Euler/boundary layer code MSES (Drela 1990). The flow was computed for the DSA-9A airfoil at $M_{0.65R} = 0.28$ and $Re_{0.65R} = 4.51 \times 10^5$. The conditions are based on the rotating speed at 65% radius and the PSP data point presented in Fig. 18 to allow direct comparison. In the code, transition is predicted via the e^N -envelope method and the critical N -factor used is $N_{\text{cr}} = 6$ as suggested by Lang et al. (2015). Computations were performed for various angles of attack α and the best fit between experimental and calculated pressures was found at $\alpha = 4.2^\circ$ (see Fig. 18). The MSES simulation predicts a pressure discontinuity at $x/c = 0.19$ due to BL transition matching the experimental findings. Deviations to the PSP results are less than $\Delta c_p \sim 0.1$ for the most part of the chord. Note the last 5% chord where the pressure increase indicated by PSP appears unphysical. The exact reasoning for the latter remains unclear, yet possible causes include incorrect assumptions for temperature or shape deviations between the actual and the theoretical trailing edge contour.

The simulation suggests that in general surface pressures are prone to exceed p_∞ near the trailing edge on the suction side of the DSA-9A airfoil causing values of $c_p > 0$. The

effect can be attributed to the tabbed contour (Fig. 9). It is also observed in Fig. 17 and appears to be even more pronounced at higher radii (see Fig. 16). Gardner and Richter (2015) and Richter et al. (2016) also measured pressures corresponding to $c_p > 0$ near the trailing edge on the same airfoil. In both studies, it was observed that the spatial extent for values of $c_p > 0$ expands towards chord-wise locations further upstream at decreasing incident angles. These findings match the qualitative radial trend displayed in the pressure maps in Fig. 16. Here, the surface area corresponding to $p/p_\infty > 1$ expands to chord-wise positions further upstream when examining the blade at increasing radii where it is assumed that the angle of incidence decreases due to the blade twist and tip effects. Still, a possible under-compensation of temperature using the approximation from Sect. 4.2 would also result in overestimated pressure values as discussed in Sect. 5.4. Because the exact radial angle of attack distribution is unknown, a quantitative discussion of the values corresponding to $p/p_\infty > 1$ is not feasible.

5.2 Variation of collective pitch

The variation of collective pitch angles from $\beta_{\text{root}} = 8.6^\circ$ to -28.8° at $f_{\text{rotor}} = 23.6$ Hz reveals interesting PSP results. The pressure map at $\beta_{\text{root}} = 24^\circ$ is displayed at the top of Fig. 20. It exhibits principally the same features as discussed above in Fig. 16. In contrast, the topology of the PSP result at $\beta_{\text{root}} = 28^\circ$ on the bottom of Fig. 20 reveals remarkable differences. The tip vortex is less pronounced and the pressure pattern is significantly altered between $0.65 < r/R < 0.9$. Especially in the region between $0.7 < r/R < 0.8$, the suction peak diminishes almost completely as compared to the case at $\beta_{\text{root}} = 24^\circ$. Moreover, oblique pressure gradients appear between $0.6 < r/R < 0.7$ and $0.8 < r/R < 0.85$ on the blade. The

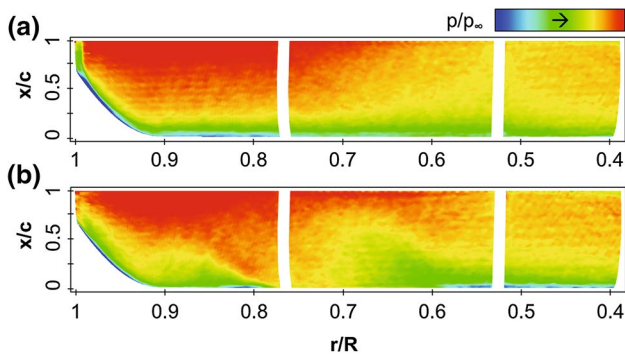


Fig. 20 Pressure topology (ensemble averaged) for $f_{\text{rotor}} = 23.6$ Hz at $\beta_{\text{root}} = 24^\circ$ (a) and 28° (b). Data correspond to points highlighted by blue squares (a) and red diamonds (b) in Figs. 21, 22

observed three-dimensional features at $\beta_{\text{root}} = 28^\circ$ in the ensemble-averaged results are caused by stalled flow. Therefore, the offset correction according to Eq. (5) was omitted because the assumed linear pressure development between the Kulite sections is infringed. Moreover, both corrective measures applied, the temperature correction via Eq. (4) as well as the subtracted influence of the internal Kulite heating do not resemble the appropriate physical behavior under stalled flow conditions due to differently balanced convective heat transfer as compared to the attached flow scenario. Hence, a quantitative discussion is omitted yet the results are well suited for qualitative comparison as data acquisition and processing is identical for the cases presented.

Stalled flow conditions at $\beta_{\text{root}} = 28^\circ$ are confirmed by the integral thrust measured by the piezo-balance. The polar in Fig. 21 exhibits the expected increase in thrust up to a collective pitch angle of $\beta_{\text{root}} = 26^\circ$, where it reaches the maximum blade loading coefficient (according to Leishman 2006) of $C_T/\sigma = 0.165$. At $\beta_{\text{root}} \geq 28^\circ$ the thrust exceeds its maximum and the standard deviation is almost doubled as indicated by the bar sizes denoting at least partially stalled flow. A similar maximum as well as the overall high standard deviations were previously measured by Schwermer et al. (2017) investigating the same configuration. They attributed the high level of fluctuations to the recording of inertial forces due to mechanical system vibrations of the test stand.

The findings are complemented by time-averaged Kulite recordings at the conditions corresponding to the colored symbols in Fig. 21. For $\beta_{\text{root}} = 20, 24$ and 28° the mean pressures are plotted as chord-wise c_p -distributions in Fig. 22 with bars indicating the standard deviation σ_{c_p} . For

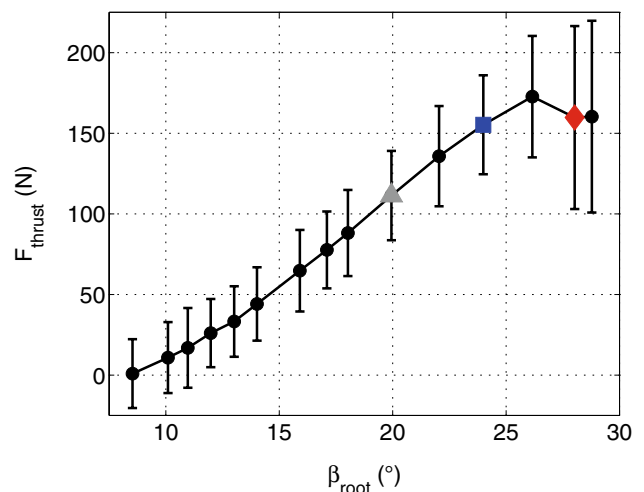


Fig. 21 Thrust polar at $f_{\text{rotor}} = 23.6$ Hz for various β_{root} , bars indicate standard deviation of a time series of 10 s sampled at 200 kHz

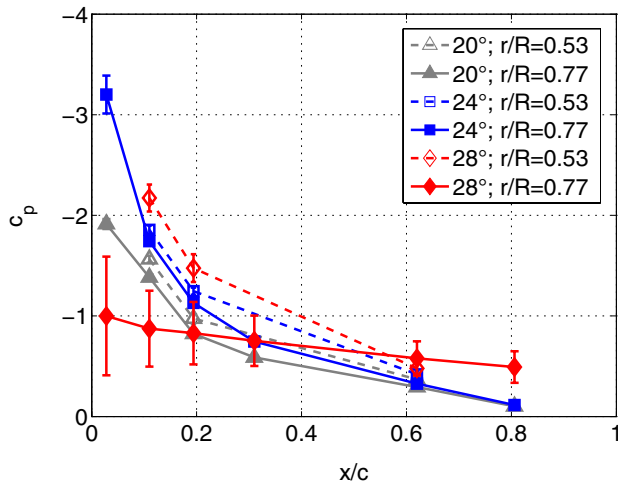


Fig. 22 Kulite data at $f_{rotor} = 23.6$ Hz for different β_{root} . Symbol- and color-coding correspond to data points highlighted in Fig. 21

$\beta_{root} = 20^\circ$ and 24° , the pitch angle increase results in stronger suction especially close to the leading edge at both radial sections. The data at $\beta_{root} = 28^\circ$ and $r/R = 0.53$ follows the trend prescribed above indicating increased suction as compared to the lower pitch angles. In contrast, at $r/R = 0.77$ the c_p -distribution is characterized by remarkably higher pressures close to the leading edge accompanied by almost no pressure recovery further downstream. The resulting “plateau-type” distribution correlates with significantly increased values of σ_{c_p} which is characteristic for stalled flow (Lorber and Carta 1988; Gardner et al. 2016). Note the significantly greater difference in standard deviation between attached and stalled flow regions for the pressure sensors as compared to the balance data in Fig. 21, because the former capture aerodynamic fluctuations only.

Considering the presented pressure maps obtained by PSP in conjunction with the force balance and Kulite measurements, it is concluded that the pressure topology at $\beta_{root} = 28^\circ$ is influenced by partially stalled flow for $r/R > 0.6$.

5.3 Pressure fluctuation analysis

The unsteady Kulite signal at $r/R = 0.77$ and $x/c = 0.028$ is investigated for the cases at $\beta_{root} = 24^\circ$ and 28° . The time series of the pressure fluctuations p' and the corresponding amplitude spectra are plotted in Fig. 23a, b. The signals shown are conditioned by a 500-Hz Butterworth low-pass filter. The spectra are obtained from a fast-Fourier transformation (FFT) of the Hanning-windowed time series. The overall stronger pressure fluctuations in the time signal at $\beta_{root} = 28^\circ$ reflect the difference in σ_{c_p} as observed in Fig. 22. The corresponding spectrum below denotes comparatively

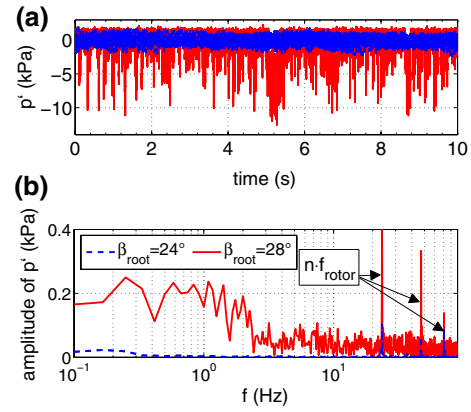


Fig. 23 Time series (a) and amplitude spectra (b) of pressure fluctuations measured by Kulite at $x/c = 0.028$; $r/R = 0.77$ and $f_{rotor} = 23.6$ Hz. Signals are low-pass filtered at 500 Hz. Colors as in Figs. 21, 22

higher amplitudes especially at low frequencies, below 2–3 Hz. Note that in both signals the highest amplitudes are contained in the rotating frequency and its higher harmonics. This is due to the rotor support downstream and in the wake of the rotor disc causing an upstream pressure change once per revolution for the blade equipped with pressure sensors. The effect is therefore also present under the attached flow condition at $\beta_{root} = 24^\circ$, where all other frequencies exhibit negligible amplitudes.

Whereas conventional phase-averaging methods are in principle limited to resolving periodic phenomena, a great advantage of the single-shot lifetime technique is that it allows to capture random, i.e. broadband pressure fluctuations. Presuming that the camera is at rest, transient phenomena are sampled every n th blade revolution depending on the system limit with respect to the data acquisition rate and the time response of the paint. In order to extract information on pressure fluctuations from the data available the measured standard deviation in pressure is evaluated according to

$$\frac{\sigma_{p'}}{\rho_\infty} = \frac{1}{s_{p,ref}} \cdot \frac{\sqrt{\sigma_{R_{wind-on}}^2 - \sigma_{R_{wind-off}}^2}}{\bar{R}_{wind-off}} \quad (7)$$

In this equation σ_R is the standard deviation of all 128 wind-on and wind-off ratio images, respectively, and $s_{p,ref}$ is the pressure sensitivity at reference conditions (100 kPa, 20°). In the expression above, it is assumed that $\sigma_{R_{wind-on}}$ contains residual noise from image acquisition and processing which is superposed to the signal variations due to oscillating pressure. Therefore, $\sigma_{R_{wind-off}}$ is subtracted since the wind-off ratio images are acquired at constant pressure and thus contain residual noise only.

The resulting standard deviations at $f_{rotor} = 23.6$ Hz and $\beta_{root} = 24^\circ$ such as at 28° are displayed in Fig. 24a, b,

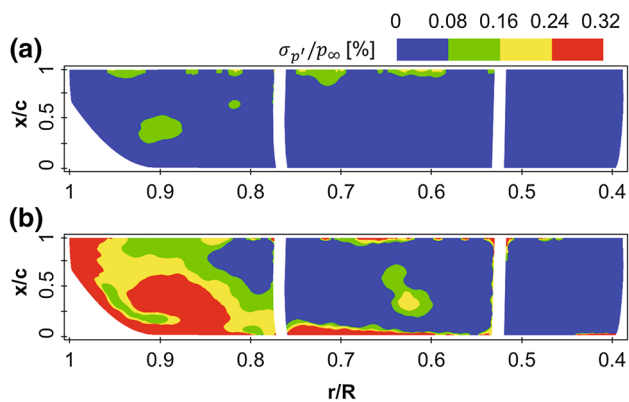


Fig. 24 Measured relative standard deviation of pressure according to Eq. (7) for $f_{\text{rotor}} = 23.6$ Hz; $\beta_{\text{root}} = 24^\circ$ (a) and 28° (b)

respectively. As opposed to the case at $\beta_{\text{root}} = 24^\circ$ significantly stronger pressure fluctuations appear at $\beta_{\text{root}} = 28^\circ$. They can be deduced along the leading edge starting from $r/R > 0.6$ all the way to the blade tip, where the footprint of the tip vortex was previously identified (see Fig. 20). The finding seems reasonable presuming that it constitutes the area where the flow detaches causing blade loading fluctuations and thus a transient behavior of the tip vortex as well. Letzgun et al. (2016) simulated the same rotor model configuration at cyclic pitch variation. In their study, stall onset was detected by finding incipient vortex shedding starting from the leading edge at 80–90% radius which is where transient flow is detected here. In Fig. 24b, strong pressure fluctuations can be distinguished in the form of an oblique patch between $0.8 < r/R < 0.9$. It is accompanied by a smaller area between $0.6 < r/R < 0.65$ which also denotes increased oscillations. Note that these patterns occur approximately where oblique pressure gradients can be deduced from the corresponding ensemble-averaged pressure result in Fig. 20b. Similar oblique patterns were detected by Disotell et al. (2014) on helicopter blades in forward flight, who attributed the finding to the effect of centrifugal forces on detached flow structures as previously studied by Raghav and Komerath (2013).

It should be noted that the paint used in this study [PtTFPP in poly(4-TBS)] is mainly designed for steady-state measurements. Though the time response is not measured explicitly here, it is expected to be in the order of several hertz similar to other polymer-based PSPs (Winslow et al. 1996). Thus, it is believed that mainly the increased low-frequency amplitudes are contained in the result shown in Fig. 24. In addition, higher-frequency fluctuations (above 5–10 Hz) are smeared out which complicates a precise distinguishability between stalled and attached flow regions in the result shown. For more sophisticated investigations, the measurement system dynamics should be improved especially in terms of the time response of the paint. For instance,

fast-responding PSPs have successfully been applied to capture transient pressure phenomena on model helicopter rotor blades in forward flight (Disotell et al. 2014; Watkins et al. 2016). Still, the results presented in this study underline the potential of the single-shot lifetime technique to investigate stalled flow on fast rotating blades.

5.4 Measurement uncertainty

The uncertainty remaining from uncorrected temperature ranges from 0.5 to 0.8 kPa/K with increased sensitivity at higher pressures and lower temperatures occurring closer to the rotor hub. In this work, the maximum deviation between valid TSP data and the adiabatic wall temperature is found to be ~ 2.5 K in radial direction. An uncertainty in this range corresponds to an error in pressure between 1 and 2% of p_∞ in blade radial direction depending on the temperature between the tip and the hub, respectively. Even if temperature effects are appropriately corrected for, the limiting error source in that case is due to photon noise in the acquired images. According to the method proposed by Liu and Sullivan (2005) for the gated-lifetime approach this uncertainty ranges approximately from 1.4 to 2.3% for the single-shot results. The variation is due to the variability of pressure-sensitivity with temperature and pressure as well as due to the inhomogeneous signal intensity across the blade span. Ensemble averaging of 128 images reduces this uncertainty to 0.1–0.2% corresponding to 100–200 Pa according to the test conditions in this work.

In general, all error sources in PSP measurements are included when comparing the data to reference measurements such as the fast response pressure transducer readings in this study. In view of the above-mentioned difficulties in the vicinity of the Kulite sections (see Sect. 4.3), PSP data are extracted at $r/R = 0.65$ and compared to the mean of pressure tap data at the same chord-wise locations but at 53 and 77% radius, respectively. After applying the offset according to Eq. (5), the residual deltas are evaluated at each chord-wise location and for all data points but the one, where stalled flow is detected. The root-mean-square level of the residual deltas is ~ 250 Pa. Because the value is based on the assumption of linear pressure evolution in between the Kulite sections and includes all possible error sources (see Liu and Sullivan 2005), it is reasonable that the more restrictive and theoretical photon-noise approximation from above is exceeded.

6 Concluding remarks

In this work, the application of an optimized image acquisition technique for surface pressure measurements on fast rotating blades is presented.

The measurement system characteristics are assessed and the technique is demonstrated to solve the problem of image blur when applied to fast rotating blades. Being directly implemented in the camera employed, the optimized technique allows omitting error-prone post-processing routines or laborious setups to eliminate artifacts originating from rotational blur. The system is successfully applied to measure surface pressures on the suction side of a Mach-scaled helicopter blade under axisymmetric flow conditions similar to climb at various collective pitch settings and blade tip Mach and chord Reynolds numbers of $M_{\text{tip}} = 0.29 - 0.57$ and $Re_{\text{tip}} = 4.63 - 9.26 \times 10^5$.

Resulting surface pressure maps exhibit plausible trends at varying rotation rates and collective pitch angles. The results reveal flow features such as the footprint of the tip-vortex and the suction peak parallel to the leading edge. A “best-practice” comparison between ensemble-averaged PSP data and fast-response pressure tap readings reveals an RMS-level of residual deltas of ~ 250 Pa. Sample PSP results reveal a chord-wise pressure discontinuity just downstream of the suction peak. Detailed analysis and comparison to results of a separately conducted TSP experiment to measure boundary-layer transition prove the correlation between the observed “kink” in the PSP results and the abrupt pressure increase indicative for laminar–turbulent transition on the airfoil investigated. To the authors’ knowledge this is the first published work where BL transition could be distinguished in PSP data on fast rotating blades emphasizing the capability of the optimized measurement technique to capture spatial pressure gradients in a precise manner. A solution computed by the 2D coupled Euler/ boundary-layer code MSES is compared to the measured surface pressures and agrees within $\Delta c_p \sim 0.1$ supporting the plausibility of the experimental findings. Partially stalled flow is detected for a particular case and the single-shot lifetime technique applied allows to identify stall-related, low-frequency pressure fluctuations.

The biggest potential for improvement in further studies originates from the temperature sensitivity of the PSP employed. The reported difficulties with respect to the correction of temperature effects are believed to be tackled most efficiently by measuring the temperature of the PSP-coated blade surface directly. This could be realized by infrared imaging, yet facing the challenge to capture sufficient signal and to avoid image blur. A different solution is the use of a dual-type paint allowing to capture pressure- and temperature-sensitive signals in parallel. Peng et al. (2013) recently presented an approach in this respect, yet needing further development to be suitable for lifetime measurements on fast rotating blades.

Acknowledgements The assistance of M. Krebs, A. D. Gardner, J. Braukmann and M. Hilfer (all DLR Göttingen) during preparation and

execution of the measurements as well as the fruitful discussions with A. D. Gardner and S. Schaber (Airbus) are gratefully acknowledged.

References

- Ashill P, Betts C, Gaudet I (1996) A wind tunnel study of transition flows on a swept panel wing at high subsonic speeds. In: CEAS 2nd European Forum on Laminar Flow Technology, AAAF, pp 10.1–10.17
- Balch DT, Lombardi J (1985) Experimental study of main rotor tip geometry and tail rotor interaction in hover. vol i—text and figures. Contractor Report 177336, NASA
- Bell JH, Schairer ET, Hand LA, Mehta RD (2001) Surface pressure measurements using luminescent coatings. *Annu Rev Fluid Mech* 33(1):155–206. doi:10.1146/annurev.fluid.33.1.155
- Bencic T (1997) Rotating pressure measurements on a scale model high-by-pass ratio fan using PSP at NASA LeRC. In: Proceedings of the 5th Annual Pressure Sensitive Paint Workshop, Arnold Engineering Development Center, Tullahoma, Tennessee
- Bickel G, Häusler G, Maul M (1985) Triangulation with expanded range of depth. *Opt Eng* 24(6):975–977. doi:10.1117/12.7973610
- Disotell KJ, Peng D, Juliano TJ, Gregory JW, Crafton JW, Komerath NM (2014) Single-shot temperature- and pressure-sensitive paint measurements on an unsteady helicopter blade. *Exp Fluids* 55(2):1671. doi:10.1007/s00348-014-1671-2
- Drela M (1990) Newton solution of coupled viscous/inviscid multi-element airfoil flows. In: 21st Fluid Dynamics, Plasma Dynamics and Lasers Conference, Seattle, WA, AIAA 90-1470. doi:10.2514/6.1990-1470
- Eckert ERG (1962) Survey on heat transfer at high speeds. Tech. Rep. ARL 189, Aeronautical Research Laboratory, US Air Force
- Fey U, Egami Y (2007) Transition detection by temperature-sensitive paint. *Springer handbook of experimental fluid mechanics*, vol 7.4. Springer, Berlin
- Gardner AD, Richter K (2015) Boundary layer transition determination for periodic and static flows using phase-averaged pressure data. *Exp Fluids* 56(6):119. doi:10.1007/s00348-015-1992-9
- Gardner AD, Wolf CC, Raffel M (2016) A new method of dynamic and static stall detection using infrared thermography. *Exp Fluids* 57(9):149. doi:10.1007/s00348-016-2235-4
- Geisler R (2014) A fast double shutter system for ccd image sensors. *Meas Sci Technol* 25(2):025,404. doi:10.1088/0957-0233/25/2/025404
- Geisler R (2017a) A fast double shutter for ccd-based metrology. In: Shiraga H, Etoh TG (eds) Selected Papers from the 31st International Congress on High-Speed Imaging and Photonics, SPIE, Osaka, Japan, vol 10328, p 1032809. doi:10.1117/12.2269099
- Geisler R (2017b) A fast multiple shutter for luminescence lifetime imaging. *Meas Sci Technol*. doi:10.1088/1361-6501/aa7aca (in press)
- Gorton SA, Poling DR, Dadone L (1995) Laser velocimetry and blade pressure measurements of a blade vortex interaction. *J Am Helicopter Soc* 40(2):15–23. doi:10.4050/JAHS.40.15
- Gregory JW (2004) Porous pressure-sensitive paint for measurement of unsteady pressures in turbomachinery. In: 42nd AIAA Aerospace Sciences Meeting and Exhibit, Reno, NV, AIAA 2004-294. doi:10.2514/6.2004-294
- Gregory JW, Kumar P, Peng D, Fonov S, Crafton J, Liu T (2009) Integrated optical measurement techniques for investigation of fluid-structure interactions. In: 39th AIAA Fluid Dynamics Conference, San Antonio, Texas, AIAA 2009-4044. doi:10.2514/6.2009-4044
- Gregory JW, Disotell KJ, Peng D, Juliano TJ, Crafton J, Komerath NM (2014a) Inverse methods for deblurring pressure-sensitive

- paint images of rotating surfaces. *AIAA J* 52(9):2045–2061. doi:[10.2514/1.J052793](https://doi.org/10.2514/1.J052793)
- Gregory JW, Sakaue H, Liu T, Sullivan JP (2014b) Fast pressure-sensitive paint for flow and acoustic diagnostics. *Annu Rev Fluid Mech* 46(1):303–330. doi:[10.1146/annurev-fluid-010313-141304](https://doi.org/10.1146/annurev-fluid-010313-141304)
- Hariharan NS, Egolf TA, Sankar LN (2014) Simulation of rotor in hover: Current state, challenges and standardized evaluation. In: 52nd Aerospace Sciences Meeting, National Harbor, Maryland, AIAA 2014-0041. doi:[10.2514/6.2014-0041](https://doi.org/10.2514/6.2014-0041)
- Juliano TJ, Kumar P, Peng D, Gregory JW, Crafton J, Fonov S (2011) Single-shot, lifetime-based pressure-sensitive paint for rotating blades. *Meas Sci Technol* 22(8):08,5403. doi:[10.1088/0957-0233/22/8/085403](https://doi.org/10.1088/0957-0233/22/8/085403)
- Juliano TJ, Disotell KJ, Gregory JW, Crafton J, Fonov S (2012) Motion-deblurred, fast-response pressure-sensitive paint on a rotor in forward flight. *Meas Sci Technol* 23(4):04,5303. doi:[10.1088/0957-0233/23/4/045303](https://doi.org/10.1088/0957-0233/23/4/045303)
- Klein C, Engler RH, Henne U, Sachs WE (2005) Application of pressure-sensitive paint for determination of the pressure field and calculation of the forces and moments of models in a wind tunnel. *Exp Fluids* 39(2):475–483. doi:[10.1007/s00348-005-1010-8](https://doi.org/10.1007/s00348-005-1010-8)
- Klein C, Henne U, Sachs W, Hock S, Falk N, Beifuss U, Ondrus V, Schaber S (2013) Pressure measurement on rotating propeller blades by means of the pressure-sensitive paint lifetime method. In: 51st AIAA Aerospace Sciences Meeting including the New Horizons Forum and Aerospace Exposition, Grapevine, TX, AIAA 2013-0483. doi:[10.2514/6.2013-483](https://doi.org/10.2514/6.2013-483)
- Kreplin HP, Höhler G (1992) Application of the surface hot film technique for laminar flow investigations. In: 1st European Forum on Laminar Flow Technology, Deutsche Gesellschaft für Luft- und Raumfahrt, Hamburg, pp 123–131
- Lang W, Gardner AD, Mariappan S, Klein C, Raffel M (2015) Boundary-layer transition on a rotor blade measured by temperature-sensitive paint, thermal imaging and image derotation. *Exp Fluids* 56(6):118. doi:[10.1007/s00348-015-1988-5](https://doi.org/10.1007/s00348-015-1988-5)
- Leishman JG (2006) Principles of helicopter aerodynamics. Cambridge University Press, Cambridge
- Letzjus J, Keßler M, Krämer E (2016) CFD-simulation of three-dimensional dynamic stall on a rotor with cyclic pitch control. In: 41th European Rotorcraft Forum 2015, Deutsche Gesellschaft für Luft- und Raumfahrt, Munich
- Liu T, Sullivan JP (2005) Pressure and temperature sensitive paints. Springer, Berlin
- Lorber PF, Carta FO (1988) Airfoil dynamic stall at constant pitch rate and high Reynolds number. *J Aircr* 25(6):548–556. doi:[10.2514/3.45621](https://doi.org/10.2514/3.45621)
- Lorber PF, Stauter RC, Landgrebe AJ (1989) A comprehensive hover test of the airloads and airflow of an extensively instrumented model helicopter rotor. In: 45th Annual Forum of the American Helicopter Society, AHS International, Boston, MA
- Mahalingam R, Wong O, Komerath N (2000) Experiments on the origin of tip-vortices. In: 38th Aerospace Sciences Meeting and Exhibit, Reno, NV, AIAA 2000-0278. doi:[10.2514/6.2000-278](https://doi.org/10.2514/6.2000-278)
- McLachlan B, Bell J (1995) Pressure-sensitive paint in aerodynamic testing. *Exp Thermal Fluid Sci* 10(4):470–485. doi:[10.1016/0894-1777\(94\)00123-P](https://doi.org/10.1016/0894-1777(94)00123-P)
- Mebarki Y, Benmeddour A (2016) Pressure-sensitive paint measurements on a moving store in the NRC 1.5 m blowdown wind tunnel. In: 32nd AIAA Aerodynamic Measurement Technology and Ground Testing Conference, Washington, DC, AIAA 2016-4161. doi:[10.2514/6.2016-4161](https://doi.org/10.2514/6.2016-4161)
- Pandey A, Gregory JW, Stanfield S, Crafton JW (2016) Comparison of blur elimination techniques for PSP images of rotating surfaces. In: 54th AIAA Aerospace Sciences Meeting, San Diego, CA, AIAA 2016-2019. doi:[10.2514/6.2016-2019](https://doi.org/10.2514/6.2016-2019)
- Peng D, Jensen CD, Juliano TJ, Gregory JW, Crafton J, Palluconi S, Liu T (2013) Temperature-compensated fast pressure-sensitive paint. *AIAA J* 51(10):2420–2431. doi:[10.2514/1.J052318](https://doi.org/10.2514/1.J052318)
- Popov AV, Botez RM, Labib M (2008) Transition point detection from the surface pressure distribution for controller design. *J Aircr* 45(1):23–28. doi:[10.2514/1.31488](https://doi.org/10.2514/1.31488)
- Puklin E, Carlson B, Gouin S, Costin C, Green E, Ponomarev S, Tanji H, Gouterman M (2000) Ideality of pressure-sensitive paint. I. platinum tetra(pentafluorophenyl)porphine in fluoroacrylic polymer. *J Appl Polym Sci* 77(13):2795–2804. doi:[10.1002/1097-4628\(20000923\)77:13<2795::AID-APP1>3.0.CO;2-K](https://doi.org/10.1002/1097-4628(20000923)77:13<2795::AID-APP1>3.0.CO;2-K)
- Raffel M, Heineck JT (2014) Mirror-based image derotation for aerodynamic rotor measurements. *AIAA J* 52(6):1337–1341. doi:[10.2514/1.J052836](https://doi.org/10.2514/1.J052836)
- Raffel M, Gardner AD, Schwermer T, Merz CB, Weiss A, Braukmann J, Wolf CC (2017) Rotating blade stall maps measured by differential infrared thermography. *AIAA J*. doi:[10.2514/1.J055452](https://doi.org/10.2514/1.J055452)
- Raghav V, Komerath N (2013) An exploration of radial flow on a rotating blade in retreating blade stall. *J Am Helicopter Soc* 58(2):1–10. doi:[10.4050/JAHS.58.022005](https://doi.org/10.4050/JAHS.58.022005)
- Richter K, Wolf CC, Gardner AD, Merz CB (2016) Detection of unsteady boundary layer transition using three experimental methods. In: 54th AIAA Aerospace Sciences Meeting, San Diego, CA, AIAA 2016-1072. doi:[10.2514/6.2016-1072](https://doi.org/10.2514/6.2016-1072)
- Ruyten W, Sellers M (2006) Improved data processing for pressure-sensitive paint measurements in an industrial facility. In: 44th AIAA Aerospace Sciences Meeting and Exhibit, Reno, NV, AIAA 2006-1042. doi:[10.2514/6.2006-1042](https://doi.org/10.2514/6.2006-1042)
- Schwermer T, Richter K, Raffel M (2016) Development of a rotor test facility for the investigation of dynamic stall. In: Dillmann A, Heller G, Krämer E, Wagner C, Breitsamter C (eds) New results in numerical and experimental fluid mechanics. X. Notes on numerical fluid mechanics and multidisciplinary design, vol 132. Springer, Cham, pp 663–673. doi:[10.1007/978-3-319-27279-5_58](https://doi.org/10.1007/978-3-319-27279-5_58)
- Schwermer T, Gardner AD, Raffel M (2017) Dynamic stall experiments on a rotor with high cyclic setting in axial inflow. In: AHS International's 73rd Annual Forum and Technology Display, Fort Worth, TX
- Suryanarayanan A, Ozturk B, Schobeiri MT, Han JC (2010) Film-cooling effectiveness on a rotating turbine platform using pressure sensitive paint technique. *J Turbomach* 132(4):04,1001–04,1013. doi:[10.1115/1.3142860](https://doi.org/10.1115/1.3142860)
- Tung C, Branum L (1990) Model tilt-rotor hover performance and surface pressure measurement. In: 46th Annual Forum of the American Helicopter Society, Washington DC
- Vuillet A, Allongue M, Philippe JJ, Desopper A (1989) Performance and aerodynamic development of the super puma Uk II main rotor with new SPP 8 blade tip design. In: 15th European Rotorcraft Forum, Deutsche Gesellschaft für Luft- und Raumfahrt e.V., Amsterdam
- Watkins AN, Leighty BD, Lipford WE, Goodman KZ, Crafton J, Gregory JW (2016) Measuring surface pressures on rotor blades using pressure-sensitive paint. *AIAA J* 54(1):206–215. doi:[10.2514/1.J054191](https://doi.org/10.2514/1.J054191)
- Winslow NA, Carrol BF, Setzer FM (1996) Frequency response of pressure sensitive paints. In: 27th AIAA Fluid Dynamics Conference, New Orleans, LA, AIAA 96-1967. doi:[10.2514/6.1996-1967](https://doi.org/10.2514/6.1996-1967)
- Wong OD, Watkins AN, Ingram JL (2005) Pressure sensitive paint measurements on 15% scale rotor blades in hover. In: 35th AIAA Fluid Dynamics Conference and Exhibit, Toronto, ON, AIAA 2005-5008. doi:[10.2514/6.2005-5008](https://doi.org/10.2514/6.2005-5008)
- Wong OD, Noonan KW, Watkins AN, Jenkins LN, Yao CS (2010) Non-intrusive measurements of a four-bladed rotor in hover—a first look. In: AHS Aeromechanics Specialists' Conference, San Francisco, CA

- Yamauchi GK, Johnson W (1995) Flow field analysis of a model prop rotor in hover. In: Proceedings of the 21st European Rotorcraft Forum, Deutsche Gesellschaft für Luft- und Raumfahrt, St Petersburg
- Yorita D, Asai K, Klein C, Henne U, Schaber S (2012) Transition detection on rotating propeller blades by means of temperature sensitive paint. In: 50th AIAA Aerospace Sciences Meeting including the New Horizons Forum and Aerospace Exposition, Nashville, TN, AIAA 2012-1187. doi:[10.2514/6.2012-1187](https://doi.org/10.2514/6.2012-1187)
- Yorita D, Henne U, Klein C (2017) Improvement of lifetime-based PSP technique for industrial wind tunnel tests. In: 55th AIAA Aerospace Sciences Meeting, Grapevine, TX, AIAA 2017-0703. doi:[10.2514/6.2017-0703](https://doi.org/10.2514/6.2017-0703)